Structural behavior and spin state features of BaAl2O4 scaled through tuned Co3+ doping

Journal:	*Inorganic Chemistry*
Manuscript ID	ic-2020-034754.R2
Manuscript Type:	Article
Date Submitted by the Author:	n/a
Complete List of Authors:	Vrankic, Martina; Institut Ruder Boskovic, Šarić, Ankica; Institut Ruder Boskovic, Division of Materials Chemistry Bosnar, Sanja; Institut Ruder Boskovic, Barišić, Dario; University of Zagreb, Division of experimental physics, Faculty of science and mathematics Pajić, Damir; Faculty of Science, University of Zagreb, Department of Physics Lützenkirchen-Hecht, Dirk; Bergische Universitat Wuppertal, Institut für Materialwissenschaften und Fachbereich C - Physik Jelovica Badovinac, Ivana; University of Rijeka, Department of Physics and Center for Micro- and Nanosciences and Technologies Petravic, Mladen; Sveuciliste u Rijeci, Department of Physics Altomare, Angela; Bari, Istituto di Cristallografia - Sede di Rizzi, Rosanna; Sede di Bari, Istituto di Cristallografia Klaser, Teodoro; University of Zagreb Faculty of Science Department of Physics

SCHOLARONE™
Manuscripts

Structural behavior and spin state features of

BaAl$_2$O$_4$ scaled through tuned Co^{3+} doping

Martina Vrankić,[a] Ankica Šarić,[a] Sanja Bosnar,[b] Dario Barišić,[c] Damir Pajić,[c] Dirk Lützenkirchen-Hecht,[d] Ivana Jelovica Badovinac,[e] Mladen Petravić,[e] Angela Altomare,[f] Rosanna Rizzi,[f] Teodoro Klaser[c]*

[a]Division of Materials Physics and Center of Excellence for Advanced Materials and Sensing Devices, Ruđer Bošković Institute, Bijenička 54, 10000 Zagreb, Croatia

E-mail: mvrankic@irb.hr

[b]Division of Materials Chemistry, Ruđer Bošković Institute, Bijenička 54, 10000 Zagreb, Croatia

[c]Department of Physics, Faculty of Science, University of Zagreb, Bijenička 32, 10000 Zagreb, Croatia

[d]Fk. 4, Physik, Bergische Universität Wuppertal, Gauss-Straße 20, D-42097 Wuppertal, Germany

[e]Department of Physics and Centre for Micro- and Nanosciences and Technologies University of Rijeka, Radmile Matejčić 2, 51000 Rijeka, Croatia

[f]Institute of Crystallography-CNR, via Amendola 122/o, 70126 Bari, Italy

Abstract

Pure and Co^{3+}-doped $BaAl_2O_4$ [$Ba(Al_{1-x}Co_x)_2O_4$, $x = 0, 0.0077, 0.0379$] powder samples were prepared by a facile hydrothermal route. Elemental analyses by static Secondary Ion Mass Spectrometry (SIMS), X-ray Absorption Spectroscopy (XAS) measurements at the Co K-edge, and X-ray diffraction studies were fully correlated thus addressing a complete description of the structural complexity of Co^{3+}-doped $BaAl_2O_4$ powder. Powder X-Ray Diffraction (PXRD) patterns indicated that prepared samples were nanocrystalline of hexagonal $P6_3$ symmetry. The X-ray Absorption Near-Edge Structure (XANES) measurements revealed the presence of cobalt in a +3 oxidation state, whilst the rarely documented, tetrahedral symmetry around Co^{3+} was extracted from the Extended X-ray Absorption Fine Structure (EXAFS) oscillation patterns. Rietveld structure refinements showed that Co^{3+} preferentially substitutes Al^{3+} at tetrahedral Al3 sites of $BaAl_2O_4$ host lattice, whereas the (Al3)O_4 tetrahedra remain rather regular with Co^{3+}–O distances ranging from 1.73(9)–1.74(9) Å. The underlying magneto-structural features were unraveled through axial and rhombic zero-field splitting (ZFS) terms. The increased substitution of Al^{3+} by Co^{3+} at Al3 sites leads to an increase of the axial ZFS terms in Co^{3+}-doped $BaAl_2O_4$ powder from 10.8 to 26.3 K, whereas the rhombic ZFS parameters across the series change in the range from 2.7 to 10.4 K, showing a considerable increase of anisotropy together with the values of the anisotropic g-tensor components flowing from 1.7 to 2.5. We defined the line between the Co^{3+} doping limit and influenced magneto-structural characteristics, thus enabling the design of strategy to control the ZFS terms contributions to magnetic anisotropy within Co^{3+}-doped $BaAl_2O_4$ powder.

Keywords: Rietveld refinement, powder diffraction, Co^{3+}-doping, local atomic environment, spin state, zero-field splitting, X-ray absorption spectroscopy

1. INTRODUCTION

The demanding task of tuning the functional properties of oxide materials is governed by the idea of finding the optimal combination of their mechanical, physical, and chemical properties to systematically tailor the desired functionalities and operating conditions of the final product. Thus, in the research of metal oxides, one of the most important targets and a crucial step surely includes a thorough understanding of their characteristics. Undeniably, for a given composition, most properties show a strong dependence on the size and morphology of the nanostructures.[1-3] Assuredly, understanding the delicate synergy of thoroughly determined atomic and electronic structure, chemical composition, sufficient purity, morphology, and particle size of any material is of pivotal interest and a highly challenging multitask.

Exceptionally high thermal stability (up to 1815 °C), non-toxicity, and good dielectric, pyroelectric, and hydraulic-hardening properties make $BaAl_2O_4$ utilized in diverse production frameworks. Specifically, band-gap of E_g=6.5 eV and a small permittivity ε'= 14 at room temperature enable a strong localization of the photo-excited carriers.[4,5] These potential benefits are extensively used in the fabrication of a wide array of consumer products such as fluorescent lamps, light-emitting diodes, field emission displays, plasma display panels, fiber amplifiers, and dispenser cathodes.[6] This especially refers to doped $BaAl_2O_4$ materials as doping is a valuable strategy for modulating and/or creating new properties of a $BaAl_2O_4$ host in a controlled manner, thus offering an optimal combination of electrical, optical, and microstructural properties.[7,8] Our earlier study extended the field of $BaAl_2O_4$ applications to the oxygen-driven storage capacity of this material, initiated by the unique antiferromagnetic transition in crystalline oxygen.[9] The $BaAl_2O_4$ crystallizes in a hexagonal assembly at room temperature (RT), within $P6_3$ (space group (s. g.) no. 173 with lattice constants a = 10.449(1) Å, and c = 8.793(1) Å)[10-12] and $P6_322$ (s. g. no. 182 with lattice constants a = 5.2211(1) Å, and c = 8.7898(1) Å)[9] symmetries, respectively, depending on the subtle preparation conditions.

3

The hexagonal packing described by the space group $P6_3$ construes two different barium sites, Ba1 and Ba2, positioned on two inequivalent crystallographic sites: $2a$ and $6c$ respectively, and coordinated by nine oxygen ions with average Ba−O distances of 2.85 Å for the Ba1 and 2.95 Å for the Ba2 site. The structure complexity is further raised by four tetrahedrally coordinated aluminum sites, Al1 to Al4, with average Al−O bond-lengths of 1.77, 1.74, 1.72, and 1.80 Å, respectively, wherein two different kinds of AlO_4 tetrahedra form hexagonal channels where the large Ba^{2+} cations are located.

It is well known from the literature that the physical properties of the $BaAl_2O_4$ host can be controlled chemically and/or physically. The continuous modification of both crystal structure and electronic state by substitution of either, or both, Al and Ba cation sites[6,12-16] and/or an application of thermal treatment under reduction conditions[17-19] endow $BaAl_2O_4$ with manifold aspects of structural and optical properties and boost its technologically applicable characteristics. In particular, the oxygen-deficient $BaAl_2O_4$, prepared in an H_2 flow, shows very strong optical absorption in the spectral region from 200 to 2500 nm. Zhang *et al.* confirmed both, theoretically and experimentally, that the impurity state in the forbidden band induced by oxygen vacancies is the main reason for this unique optical performance.[17] Vacancies are among the most common point defects in metal oxide materials and are responsible for a wide range of optoelectronic phenomena. As such, their profound influence on optical properties in minerals,[20-22] intrinsic electrical conductivity in semiconducting oxides,[23-27] charge trapping in microelectronic devices,[28-31] and electron-hole recombination centers in photovoltaic or photocatalytic materials[32-34] is well-elaborated in the literature. In turn, metal oxide insulators, such as $BaAl_2O_4$, might offer even more desirable properties as they have a wide forbidden band and more complex defect structures when doped with metal cations implying different charge compensation schemes.[18,19,35] A route to the development of innovative photo-tunable electronic devices with dielectric functionalities was efficiently screened out through dielectric

4

response in $Ba(Al_{0.97}Zn_{0.03})_2O_{4-\delta d}$ reported by Nagai *et al.*[36]. Many efforts have been made to enhance the performance of $BaAl_2O_4$ by metal doping,[37-40] and yet a small number of papers gave a detailed spatial distribution of dopants within the host structure[11,12,41]. With its low dielectric constant and dielectric loss and excellent insulation properties, this weak ferroelectric[42,10]ceramic is a superior candidate to replace the traditional ferroelectric materials with high dielectric loss and high dielectric constant as multilayer ceramic capacitors (MLCCs)[41,43-46]. On the other hand, the Co-dopant is commonly used as an additive in the fabrication of MLCCs[47-50] whereas the performance and reliability of MLCCs are severely dependent on microstructural parameters (*i.e.* crystallite size and lattice strain) and doping effects.[50-52]

The literature concerning physical features of Co-doped $BaAl_2O_4$ powder is relatively scarce – with, up to our knowledge, only one discrete report being focused exclusively on optical properties of Co^{2+}-doped $BaAl_2O_4$[53]. It is, therefore, mandatory to spotlight the fundamental insights into the physically correlated structural features of Co-doped $BaAl_2O_4$ powder. Namely, the lack of a thorough understanding of the relationship between detailed crystal structure and desirable properties is still a major bottleneck in the development of materials that consolidate outstanding features and practical applications. In particular, all known extraordinary material properties of cobalt-based metal oxides including superconductivity,[54] strong thermopower,[55] and metal-insulator transitions,[56,57] highly correlate to the concept of the spin state degree of freedom of the cobalt ion[58-60]. The largest spin state variability of Co^{3+} is reported mainly for the metal oxide compounds within crystal structures where cobalt is coordinated by four to six oxygen ions.[60-64] The computation of the ZFS parameters is shaped to a large extent by the coordination of Co dopants within the host lattice. Hence, assigning the proper spin state of the Co ions as a function of their metal-oxygen bond

5

length is crucial to simplify remarkably the interpretations of the magnetic properties of Co-based compounds.

In this work, short-range structural information of Co^{3+}-doped $BaAl_2O_4$ powder samples fingerprinted by the element-specific XAS measurements were complemented with the results of the long-range ordering obtained from the PXRD measurements at RT. The extraction of the oscillatory structure from the XANES and EXAFS experiments served as a sensitive structural probe providing information on the local atomic environment in Co^{3+}-doped $BaAl_2O_4$ powder and lighting up an essentially complete description of its crystal structure. The structural data of the $BaAl_2O_4$ host lattice doped with Co^{3+}, combined with the analysis of magnetic phenomena at the microscopic level, offer a feasible elucidation of the complex magneto-structural correlations within Co^{3+}-doped $BaAl_2O_4$ powder, prepared in a controlled manner.

2. EXPERIMENTAL SECTION

2.1. Materials and Synthetic Procedures. All the reagents were used as supplied with an analytical grade without any further purification. Powder samples of $BaAl_2O_4$ doped with 0, 0.77, and 3.79 at. % Co in a relation to Al were synthesized by a facile hydrothermal method with a post-annealing treatment. The formation of the Co-doped $BaAl_2O_4$ stable solid phase had a severe limitation in achieving higher doping levels (above ca. 4 at. % Co). A high purity aluminum nitrate nonahydrate $Al(NO_3)_3 \cdot 9H_2O$ (Fisher Chemical, U.S.), was used as Al, a barium nitrate, $Ba(NO_3)_2$ (Fisher Chemical, U.S.) as Ba, and a cobalt nitrate hexahydrate, $Co(NO_3)_2 \cdot 6H_2O$ (Sigma-Aldrich, U.K.) as Co precursor, respectively. The 2-hydroxypropane-1,2,3-tricarboxylic acid, $C_6H_8O_7 \cdot H_2O$, (Kemika, Croatia), and an ammonium hydroxide, NH_3 (25 %) (Kemika, Croatia) solutions were also used for the sample preparation. In a typical synthetic procedure, stoichiometric amounts of $Al(NO_3)_3 \cdot 9H_2O$, $Ba(NO_3)_2$, and $Co(NO_3)_2 \cdot 6H_2O$ were dissolved in Milli-Q water. Prepared aqueous solutions were mixed in a

proper molar ratio and additionally homogenized by constant stirring and adding a 2-hydroxypropane-1,2,3-tricarboxylic acid, $C_6H_8O_7$. Then the excess amount of NH_3 aq. was dropwise added, mixed well after each drop until the system pH reached ~10.4. Each of the prepared precursor solutions was autoclaved at 170 °C for 24 h. Subsequently, the obtained precipitates were centrifuged and washed several times with Milli-Q water, and then dried at 60 °C. The obtained samples were heated up to 1100 °C in a suited furnace with static air at a heating rate of 10 °C/min and calcined at that temperature for 4 h. The thermal treatment afforded a pure product of an undoped $BaAl_2O_4$ as a white solid. On the other hand, after cooling down to RT, the Co^{3+}-doped $BaAl_2O_4$ samples were of a greenish-blue color showing an increase in intensities with the scaling up of the Co doping concentration level. The prepared powder samples are denoted by S0, S1, and S2.

2.2. Secondary Ion Mass Spectrometry Measurements. The solid surfaces of pure and Co^{3+}-doped $BaAl_2O_4$ samples were characterized by static SIMS, providing mass spectra with high surface sensitivity, low detection limits, and the ability to detect all elements and isotopes. The SIMS analysis was carried out in a quadrupole-type instrument (Hiden SIMS Workstation) using 3 keV O_2^+ ions and collecting positive secondary ions. Flooding of the sample surface during the measurements with 500 eV electrons was employed to neutralize the surface charging on insulating surfaces of pure and Co^{3+}-doped $BaAl_2O_4$ powder samples. Typical pressure in the analysis chamber during the measurements was in a low 10^{-8} mbar range.

2.3. X-ray Absorption Spectroscopy Studies. The Co XANES along with the EXAFS experiments were carried out at beamline 10 of the DELTA synchrotron (Dortmund, Germany), operating with ca. 100–130 mA of stored 1.5 GeV electrons and using a Si (111) channel-cut monochromator[65]. A N_2 gas-filled ionization chamber was used for the incident intensities,

7

while an Ar-filled ionization chamber was used for the beam transmitted through the fine-powdered samples. The bulk sensitive fluorescence yield in XANES measurements was detected by a silicon drift diode with a multichannel analyzer and a large area passivated implanted planar silicon (PIPS) detector. Repeated scans each of typically 1 h acquisition time were performed and averaged to improve the data statistics. For comparison, the reference spectra of a Co-metal foil and several cobalt oxides of different chemical valences and compositions (*i.e.* CoO, Co^{2+}, with 6-coordinated Co−O, Co_3O_4 with equal amounts of 4-coordinated Co^{2+} and 6-coordinated Co^{3+}, and Co_2O_3 with pure Co^{3+} and 6 oxygen neighbors) were measured. The phases and scattering amplitudes were calculated using the FEFF code,[66] *ab initio calculations*, and the Athena/Artemis software package[67] was used for the quantitative fitting of the data.

2.4. Powder X-ray Diffraction Measurements. The PXRD data at RT were collected using a Bruker D8 DISCOVER laboratory diffractometer equipped with a Cu–Kα source (λ= 1.54056 Å) and a multi-mode EIGER2 R 500K detector (Dectris, Switzerland). The PXRD patterns were collected over the 2θ angular range of 10–100° and scanned with a step size of 0.02º (2θ). All diffractograms were indexed using the N-TREOR09[68,69] procedure implemented in the EXPO software[70]. The Rietveld structure refinements were performed with the GSAS-II software[71] using pseudo-Voigt profile functions and a log interpolation background model with 9 coefficients. A starting model for the Co-doped $BaAl_2O_4$ was based on that of Huang *et al.* (ICSD card no. 75426)[10] and formula as resulted from the XAS investigations of Co-doped $BaAl_2O_4$ samples. Carefully introduced chemically specific restraints on bond distances and angles as well as constraints and equivalences were necessary to take into account the rationalization and meaningfulness of the structure assembly of samples S1 and S2. In particular, the equivalences on isotropic displacement parameter U_{iso} and *x, y, z* parameters

across data sets were selected for atoms sharing the same site symmetries (*i.e.* atoms Al3 and Co at $2b$ sites). The sum of the site occupancies of Al3 and Co atoms were fixed to unity. Isotropic displacement parameters for the same kind of atoms were constrained to have a single value and allowed to be refined freely. Exceptionally, the oxygen isotropic displacement parameters were fixed at a reasonable value ($U_{iso} = 0.012$ Å^2 corresponding to $B_{iso} = 0.95$ Å^2) with minimal effect on the reliability factor. Using predicted atomic geometries the subsequent Rietveld refinements converged readily to satisfying reliability factors (see Tables 2 and 3) and yielded final fit (see Figure 6) with 82 directly refined parameters, including 9 arising from the background function, 2 instrumental parameters (sample displacement and scaling factor), 3 lattice parameters, 65 atomic parameters (comprising of fractional coordinates, isotropic displacement parameters, and occupancies) and 3 peak shape parameters. The crystallite sizes and strains in prepared samples were calculated using the phase fit method (*i.e.* simultaneously with the Rietveld structure refinements) based on the change of the profile widths compared to a standard sample.

2.5. Magnetization Studies. Magnetic moments of pure and Co^{3+}-doped $BaAl_2O_4$ powder samples were measured with a Quantum Design MPMS-5 commercial SQUID magnetometer. The temperature-dependent magnetization curves, $M(T)$ of all prepared samples were measured in the temperature range from 2 K up to RT at a constant magnetic field of $H = 1000$ Oe, while for the $M(H)$ curves values of the magnetic field H ranged from -50 000 to +50 000 Oe at $T = 2$ K. The powder samples in the form of pressed pellets were placed directly into the measuring straw to reduce the intensity of magnetic background signals. Generally, the ZFS parameters are fundamentally tied to the coordination geometries of metal ion complexes, and as such need to be uniquely determined for the Co dopant within the $BaAl_2O_4$ host. The magnetization was modeled using the ZFS Hamiltonian[72] written as:

$$\hat{H} = \beta\,\hat{S}\cdot\overleftrightarrow{g}\cdot\vec{H} + D\,[\hat{S}_z^2 - S(S+1)/3] + E\,(\hat{S}_x^2 - \hat{S}_y^2), \qquad (1)$$

where β is the Bohr magneton, $\overleftrightarrow{g}$ is the g-tensor, $\vec{H}$ is the magnetic field vector, $\hat{S},\ \hat{S}_x,\ \hat{S}_y,\ \hat{S}_z$ are the spin operators of total spin and spin components, $S\,(S+1)$ is the spin eigenvalue of $\hat{S}^2$, whilst D and E are axial and rhombic ZFS parameters, respectively. Explicitly, the term $\hat{S}\cdot\overleftrightarrow{g}\cdot\vec{H}$ was adequately calculated by applying the following formula:

$$\hat{S}\cdot\overleftrightarrow{g}\cdot\vec{H} = H[\left(g_x\hat{S}_X\cos\varphi + g_y\hat{S}_y\sin\varphi\right)\sin\theta + g_z\hat{S}_z\cos\theta], \qquad (2)$$

i.e. we assumed the g-tensor to be diagonal. The θ and φ denote angles between the principal axis of a single crystallite and magnetic field vector. To obtain a good magnetization model it was necessary to average the magnetization contributions over all directions (*i.e.* for θ from 0 to π and φ from 0 to 2π), which means that we assumed that crystallites are oriented completely randomly.

3. RESULTS AND DISCUSSION

3.1. SIMS Fingerprint Analysis. The SIMS surface spectra were recorded to detect the elemental composition and/or the possible presence of impurities embedded during the preparation of pure (sample S0) and Co^{3+}-doped $BaAl_2O_4$ powder (samples S1 and S2). The fingerprint region of the mass spectrum between 25 and 140 amu collected from the surface of sample S1 is presented in Figure 1. The mass spectrum clearly shows the presence of all expected elements in the sample: the Al peak at 27 amu, a peak related to a stable Co isotope at 59 amu, and the isotopic pattern of Ba with seven isotopes between 134 and 138 amu, with the most abundant Ba isotope at 138 amu. The isotopic pattern ascribed to the existence of doubly charged Ba secondary ions, Ba^{2+}, is also observed around 69 amu. A part of the spectrum around the oxygen peak is not shown, as the electron flooding by itself contributes to the desorption of oxygen from the surrounding sample holder.

10
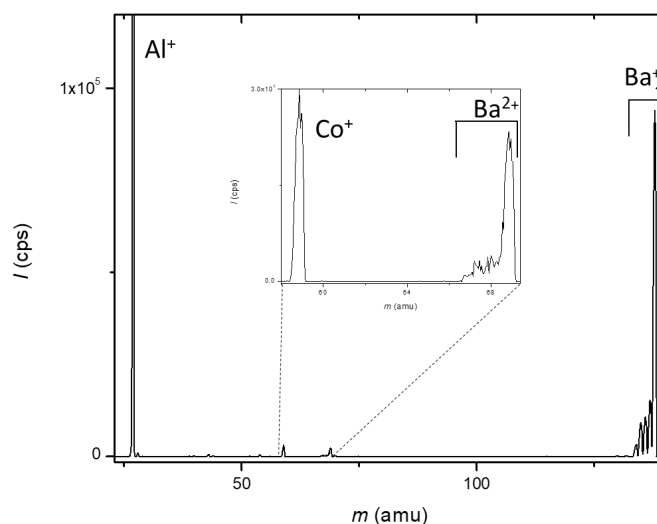
Figure 1. The positive secondary ion mass spectrum collected from the surface of sample S1. The intensities of the Co^{59} peaks measured from the surfaces of the Co^{3+}-doped $BaAl_2O_4$ samples S0, S1, and S2 are shown in Figure 2. The ratio of signal intensities scales with the expected concentration of Co in doped samples.
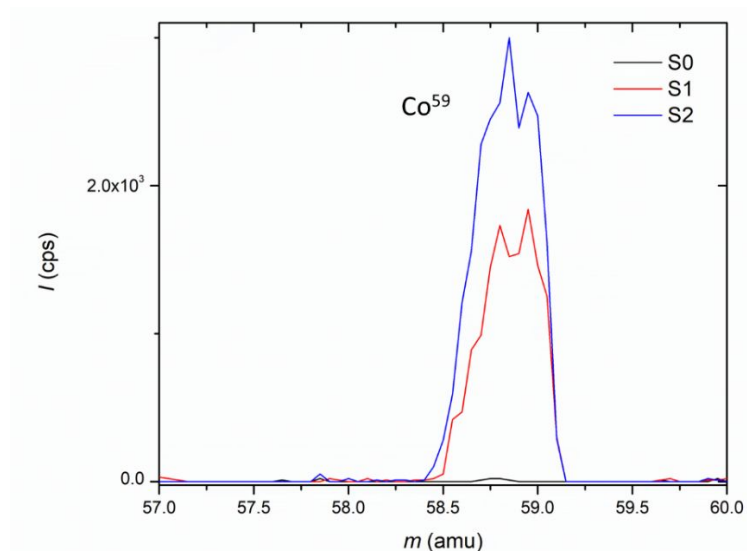
Figure 2. Comparison of the Co peak intensity in pure, S0, and Co^{3+}-doped $BaAl_2O_4$ powder samples, S1 and S2, respectively.

11

3.2. X-ray Absorption Spectroscopy. The total concentration of Co within the samples S1 and

S2 was estimated from the transmission mode X-ray absorption spectra measured at the Ba L-

edges and the Co K-edge as follows. Using the element-specific X-ray absorption cross-sections

below and above the measured X-ray absorption edges of Ba and Co, the measured change of

the absorption at the Ba- and Co-edges, and assuming the presence of stoichiometric $BaAl_2O_4$

with a density of 3.94 g/cm^3, the relative atomic concentrations of both elements can be

calculated in a straightforward manner.[73,74] Making use of $\Delta\mu_{Ba}$ = 90310 barn/atom, $\Delta\mu_{Co}$ =

30180 barn/atom, an experimentally derived edge jump of ΔA_{Ba} for Ba at the L$_3$-edge and ΔA_{Co}

for Co at the Co K-edge, the relative concentration C_{Co}/C_{Ba} can be calculated using the

following equation:

$$C_{Co}/C_{Ba} = \Delta A_{Co} / \Delta\mu_{Co} \times \Delta\mu_{Ba} / \Delta A_{Ba} \qquad (3)$$

For sample S1, the edge jump at the Ba and Co edges were determined to ΔA_{Ba} = 2.17 ± 0.1

and ΔA_{Co} = 0.039 ± 0.01, giving in total values for the concentrations of Co within sample S1

of (0.77 ± 0.12) at. % Co, and (3.79 ± 0.83) at. % Co for sample S2, respectively. It should be

mentioned that XANES spectra were also collected for sample S2, however, all the

characteristic features in the latter spectrum are substantially damped in comparison to the

XANES of sample S1, indicating the likely presence of additional Co-species in the sample S2

(see Supporting Information, Figure S1). Thus, we have focussed here on sample S1, and the

Co K-edge XANES spectrum of this sample is compared to those of several Co reference

compounds in Figure 3. As can be seen, the edge position in the spectrum of sample S1 is

substantially different from that of metallic Co and the Co^{2+}-species CoO, $Co(OH)_2$ and $CoCl_2$,

so that the presence of pure Co^{2+} in $BaAl_2O_4$ host lattice can be excluded. However, the edge

positions determined for the Co_3O_4 and Co_2O_3 are very similar, so that the discrimination of

both samples solely from the edge position appears to be difficult (inset of Figure 3).

Additionally, one may also argue that the edge position may also be influenced by the ligands

coordinated to the central element, even if the formal chemical valence of the investigated element is identical, and that it could be therefore dangerous to directly relate the edge position to the chemical valence. In the present case, *i.e.* for $BaAl_2O_4$, chemical bonds between the inserted cobalt atoms and elements other than oxygen are rather unlikely. Furthermore, Co^{2+}-species like $Co(OH)_2$, $CoCl_2$, and $Co(NO_3)_2$ with different ligands show similar edge positions compared to CoO (see the inset of Figure 3), however with different X-ray absorption near edge structures for each compound. Further variations of the edge shape and thereby the edge position may arise from changes in the entire coordination environment, *i.e.* distortions of the local atomic arrangements may shift the edge position as well. Nevertheless, the correlation of the Co-valence with the edge position of the investigated Co-dopant in the $BaAl_2O_4$ host can be used as a first estimation of the Co valence, the result of which should however carefully be discussed in terms of all characteristic features in the XANES. According to the linear regression fit of the edge positions of the reference spectra, the edge position obtained for the sample S1 (7718.2 ± 0.2 eV) is significantly larger than that obtained for all other Co^{2+} and Co^{3+} reference compounds, in particular, larger than that of Co_2O_3 with a value of 7717.6 ± 0.2 eV, and is located ideally on the linear regression, suggesting a formal Co-valence of +3. This agrees qualitatively with results recently reported by Wang and coworkers, indicating subtle but detectable differences in the edge positions of the spinel compounds $CoAl_2O_4$ (Co^{2+}), Co_3O_4 (Co^{2+}/Co^{3+}), and $ZnCo_2O_4$ (Co^{3+}), with a small positive shift of the edge with increasing Co valence as in the present case[75]. Moreover, zooming into the features detectable in the edge region of the XANES of sample S1, some pronounced features at 7720 eV and 7724 eV are clearly visible (see also Figure S1 in the Supporting Information). At the same energetic positions, weaker features are also detected in the XANES of Co_2O_3, *i.e.* Co^{3+}. Keeping in mind that Co is present in the $BaAl_2O_4$ as a dopant, inducing stress into the original structure due to *e.g.* the different size of Co and the constituents of the pristine host lattice, a more localized

13

electronic structure of the Co can be anticipated, leading to more pronounced XANES features both directly at the edge and above. Furthermore, these two edge features as well as the white line position of sample S1 at 7728.5 eV closely resemble those of $ZnCo_2O_4$ with a Co^{3+} valence (see ref. [75]), so that, in conclusion, a +3 valence of the cobalt inserted in the $BaAl_2O_4$ host appears very likely.
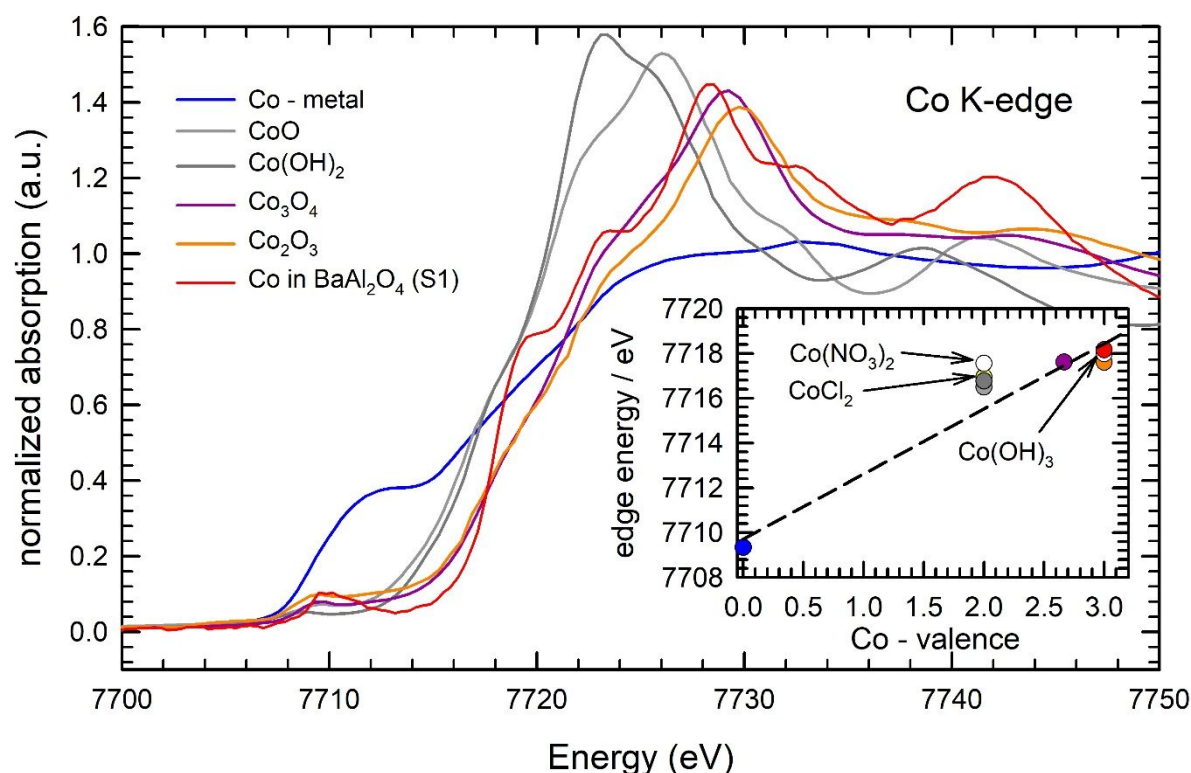
Figure 3. Comparison of the background-subtracted and normalized Co K-edge XANES spectra of sample S1, Co-metal, CoO, $Co(OH)_2$, Co_3O_4, and Co_2O_3. In the inset, the edge positions determined as the first inflection point of the spectra, are shown as a function of the formal valence of the reference samples, together with a linear regression of the data points. Edge positions from additional Co^{2+}- and Co^{3+}-species ($CoCl_2$, $Co(NO_3)_2$, $Co(OH)_3$) are included as well. From the edge position measured for the sample S1, a complete ionization of the Co atom to the +3 state can be determined.

Especially noteworthy is the versatility of the crystal structure of the $BaAl_2O_4$ host regarding the cation distribution as it features two structurally inequivalent Ba^{2+}-sites and four different Al^{3+}-sites[10,76]. While barium atoms are 9-fold coordinated with Ba–O distances ranging from 2.69 to 3.00 Å, the aluminum atoms are 4-fold coordinated with Al–O distances in the range of 1.71 to 1.83 Å. A substitution of Al^{3+} with an ionic radius of 0.39 Å by Co^{3+} within the $BaAl_2O_4$ crystal lattice appears much more likely in contrast to a substitution on regular, 9-coordinated Ba^{2+}-sites with substantially larger ionic radii. It is important to note here that the tetrahedral coordination for Co^{3+} is rarely met in reality, and when found, the Co^{3+}–O bond lengths have been reported to be in the order of 1.78–1.79 Å[77-79]. In comparison with Baker and co-workers[80], who reported the average Co^{3+}–O bond lengths of 1.88 Å for $K_5Co^{III}W_{12}O_{40}\cdot20H_2O$, Muncaster *et al.*[77] derived the considerably shorter bond distances around tetrahedrally coordinated Co^{3+} ranging from 1.7839–1.8017 Å, by simultaneously tracking the EXAFS oscillations and single-crystal X-ray diffraction data. Specifically, the high-spin Co^{3+} in a tetrahedral symmetry was found in a mixed-valence cobalt oxide $YBaCo_4O_8$.[79] However, much more structural information is required to prove these local atomic geometries. Necessarily, the contributions of the EXAFS data analysis need to be considered out as it supplies essential information on the local coordination in the Co^{3+}-doped $BaAl_2O_4$ samples. The Fourier-transform of the k^3-weighted EXAFS data $\chi(k)*k^3$ obtained from the sample S1 is presented in Figure 4.

15
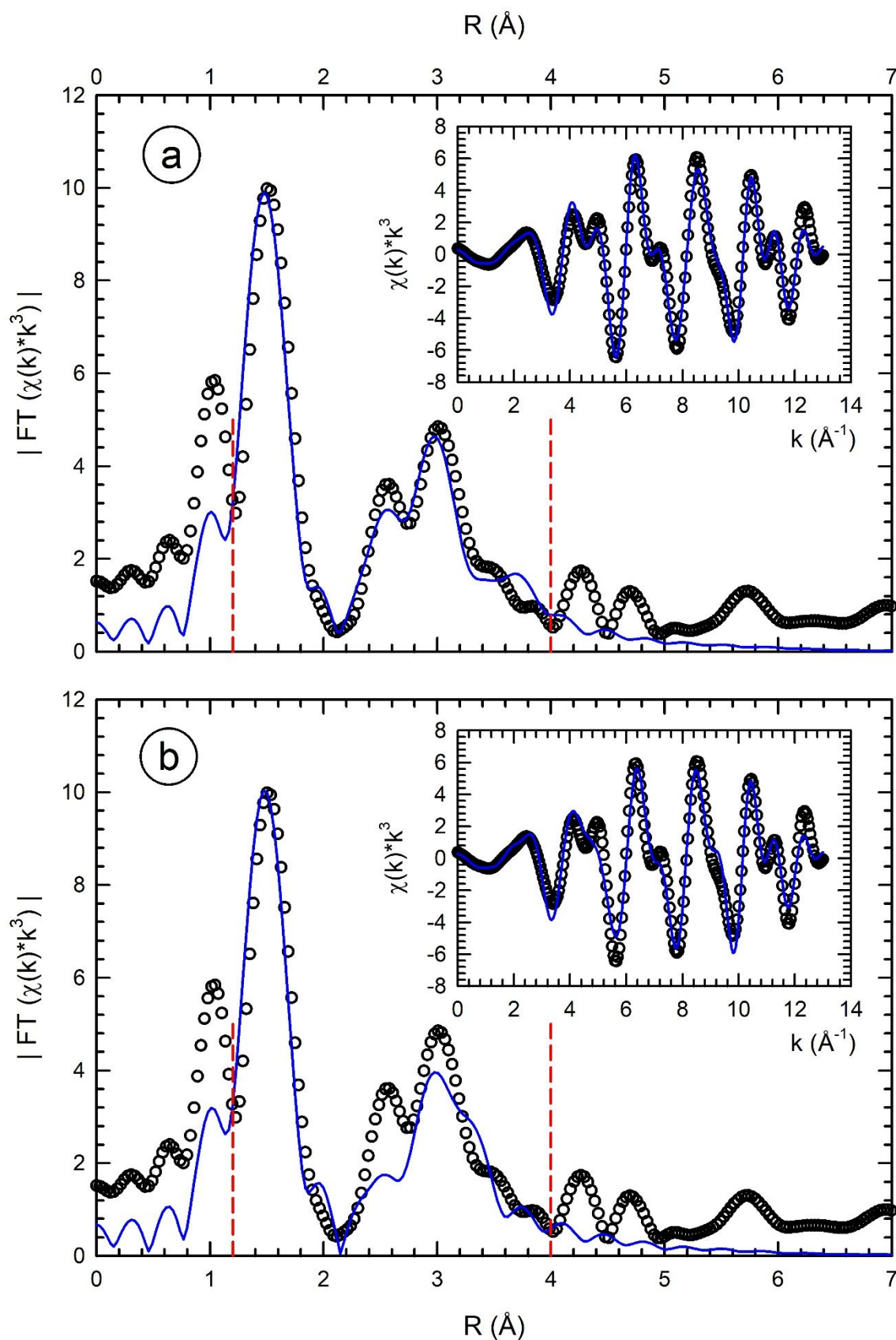
Figure 4. The magnitude of the Fourier-transform of the k^3-weighted Co K-edge EXAFS fine

structures $\chi(k)*k^3$ measured for the sample S1. (a) The experimental data (black circles) were

fitted assuming the presence of Co on regular Al3-sites within the $BaAl_2O_4$ (solid blue line), with a fit residue (*R*-factor) of 0.041. (b) Best fit of the experimental data (black circles) assuming Co on regular Al1-sites within the $BaAl_2O_4$ (solid blue line), with a fit residue of 0.075. The insets display the $\chi(k)*k^3$ for both experimental data and the fits. The *k*-range for the Fourier-transform and the R-range for the fit are 3 Å^{-1} ≤ k ≤ 12 Å^{-1} and 1.2 Å ≤ R ≤ 4 Å (vertical dashed lines), respectively.

As can be seen, there is a prominent peak at ~1.5 Å (uncorrected) radial distance, that can be related to Co−O bonds lengths, and a second distinct peak at ~3.0 Å distance, which probably originates from the Co−Ba interactions. On a first guess, only the first peak belonging to the Co−O bonds was separated using a filter function and fitted to Co−O coordination. The fit results suggest 4 nearest neighbors at a distance of 1.92 ± 0.02 Å. The obtained disorder parameter (mean square relative displacement σ^2) is rather small, with a value of 0.00153 ± 0.0005 Å^2. The values for the inner potential shift (ΔE_0) and the amplitude reduction factor (S_0^2) are well in line with the values obtained from the reference measurements for the CoO and Co_2O_3. According to the XANES measurements, Co is incorporated in the $BaAl_2O_4$ host lattice in the form of Co^{3+} ions. Such a conclusion coincides well with the values of the respective Co−O bond distances obtained for the Co-doped $BaAl_2O_4$ sample in comparison to CoO (six nearest oxygen neighbors in a distance R_1 = 2.12 ± 0.01 Å) and Co_2O_3 (six nearest neighbors with R_1 = 1.92 ± 0.01 Å) - *i.e.* the larger positive charge of the Co^{3+} leads to a shortening of the Co−O bond length, with a similar value compared to the Co^{3+}-doped $BaAl_2O_4$. For a purely tetrahedral oxygen coordination, one might expect a sharp pre-edge feature in the Co K-edge XANES of sample S1 (see Figure 3) as observed and also calculated *e.g.* for other transition metal compounds with tetrahedral environments [81,82]. The intensity of those pre-peaks is substantially affected by the details of the coordination environment, in particular, for the 3*d*

transition metals, the intensity substantially decreases in the presence of distorted tetrahedrons[83], and also for the tetrahedrally coordinated Co^{2+} in $CoAl_2O_4$, a pre-peak of rather small intensity is detected only[75]. XANES calculations for the pre-edge regions of different Co–O coordination environments employing the FEFF 8 code[84,85] indeed suggest an intense feature for Co^{3+} coordinated with 4 oxygen in an ideal tetrahedron; the peak intensity is about 40 % of the edge jump in this case (see Figure S2 in the Supporting Information). Introducing a distortion to the tetrahedral coordination with three larger and one shorter bond length as suggested by the EXAFS analysis (see below), however, the intensity drops to about 10−15 % of the edge jump and the pre-peak shifts to larger energies, well-comparable to the experimentally observed spectrum of sample S1. In contrast, an octahedral coordination leads to substantially broader pre-peaks extending over several eV between ca. 7708−7712 eV with a much smaller intensity, being in a close agreement with the experimental spectrum observed for Co_2O_3[84,85]. Therefore, as a conclusion from the first-shell EXAFS analysis and a closer inspection of the XANES pre-edge and edge features, it is very likely that a Co^{3+} species in a tetrahedral coordination environment is present for the Co-doped $BaAl_2O_4$ material. Since PXRD patterns gave no evidence for an additional Co-containing phase in samples S1 and S2, it is therefore very likely that the dopant is located on a regular lattice site within the $BaAl_2O_4$, making the four different Al-sites candidates for a Co substitution. The complexity of this peculiar crystallographic assembly is further raised by the diversity of the host wherein the positions of Al atoms result in a variety of the Al-Ba distances around ca. 3.46 Å and 3.51 Å (Al1), 3.41 Å, and 3.50 Å (Al2), 3.40 Å (Al3) and 3.51 Å for Al4, with three Ba-ions coordinated around each of the Al-sites. For photoelectron waves emerging from the X-ray absorbing Co dopant, Ba represents a strong backscattering atom, and thus, intense contributions at a larger radial distance can be expected in the Fourier-transform in comparison to Al and O in similar distances. Therefore, assuming that Co enters the host structure on an

18

Al-site, it is rather likely that the strong peak at ~3 Å radial distance in the Fourier-transform

of the Co^{3+}-doped $BaAl_2O_4$ is dominated these Co–Ba-backscattering events. Since all the

different Al-sites except Al3 have rather large Al–Ba-coordination in the range of 3.5 Å and

values of up to 4 Å, one may accordingly expect signatures in the range from 3.5 to 4.0 Å in

the Fourier-transform. Nonetheless, only the Al3 site has no coordination exceeding 3.65 Å,

thus allowing us to deductively rule out the possible location of Co on other Al sites. Due to the

absence of intense maxima in the Fourier-transform above ca. 3.5 Å, we may thus conclude that

the location of Co on Al3-sites is the most feasible one. We have therefore modeled the EXAFS

assuming such a location of the Co^{3+}-dopant within the host, and the fit results are shown as

blue lines in Figure 4 (a) in both *R*-space and back-transformed into *k*-space. Having in mind

the difficulties of the experiment, the fit with an *R*-factor of 0.041 can be considered as

reasonable. Details are compiled in Table 1. The calculated cluster comprised 16 different

atoms, resulting in a total of 12 different scattering paths included in the fit (see Table 1). From

the *k*- and *R*-ranges used for the fit, the number of independent points results in 15.7, *i.e.* it is

thus recommended that the total number of fit variables is substantially less to obtain a

statistically sound and well-justified result. We have therefore assumed global values for S_0^2

(the so-called amplitude reduction factor) and ΔE_0 (the inner potential shift), which may arise

from the choice of the exact edge position in the data. As a starting point for ΔE_0, we have used

the first inflection point of the spectrum, as displayed in the inset of Figure 3. Furthermore, the

distances of the oxygen atoms O1 and O2 with the shortest Co−O bond length as well as Ba1

(see Table 1) were individually fitted, as those are closest to the Co^{3+} dopant and thus very

sensitively towards the exact position of the dopant within the host lattice. All other bond

distances compiled in Table 1 were described by a lattice expansion factor of the entire lattice

of the Co^{3+}-doped $BaAl_2O_4$, allowing thus to model a large number of coordinations with just

one single parameter, thereby reducing the number of fit variables considerably. Besides, three

independent values were optimized for the disorder (thermal and static) of Co−O, Co−Al, and Co−Ba bond distances, to account for different vibrational properties of the three different ligand atoms. In total, thus, 9 fit variables were used, and the obtained results are compiled in Table 1.

Table 1. Results of the fit against EXAFS data for the sample S1. It is assumed for the fit that Co atom is located on the Al3-site within the $BaAl_2O_4$ host lattice, and the original distances (R_{eff}), as well as the number of atoms in the respective shells (N_i), are indicated. The global parameters S_0^2 and ΔE_0 for the EXAFS fit are (0.74 ± 0.06) and (-2.54 ± 0.94) eV, respectively. The labels of the scattering path represent the scattering atom in a distance R. If two-atom labels are provided, then the related scattering bath belongs to multiple scattering events with the respective elements.

Atom	N_i	$\sigma^2 (10^{-3}\ \text{Å}^2)$	$R(\text{Å})$	$R_{eff}(\text{Å})$
O1	3	0.42 ± 0.1	1.92(1)	1.726
O2	1	0.42 ± 0.1	1.83(1)	1.785
O3	1	1.04 ± 0.1	3.04(1)	2.972
O1 O1	6	1.24 ± 0.1	3.21(1)	3.143
Al1	3	0.88 ± 0.1	3.24(1)	3.170
O1 O2	6	1.24 ± 0.1	3.25(1)	3.183
Ba1	3	3.65 ± 0.1	3.23(1)	3.403
O1 Al1	6	1.24 ± 0.1	3.42(1)	3.346
O2 Al2	2	1.24 ± 0.1	3.51(1)	3.438
Al2	1	0.88 ± 0.1	3.51(1)	3.438
O2 Al2 O2	1	1.52 ± 0.1	3.51(1)	3.438
O4	3	0.88 ± 0.1	3.73(1)	3.637

It should be pointed out, that not only direct single scattering events were included in the fits, but also multiple scattering substantially contributed to the measured EXAFS fine structure, in agreement with the EXAFS experiments on pure and Eu-doped $BaAl_2O_4$[12]. For example, double

oxygen scattering occurs at ca. 3.21 Å and 3.25 Å, and scattering between oxygen and aluminum were detected at ca. 3.42 Å and 3.51 Å, as well as a triangular O−Al−O scattering was observed at 3.51 Å, respectively. Furthermore, the original distances of the pristine, undoped $BaAl_2O_4$ lattice are only given for comparison. The structural data used for the refinement of the EXAFS data fits (i.e. the initial model) were different from these R_{eff} values, resulting in more precise estimations of EXAFS phases and amplitude functions for the fits. For comparison, the best fit obtained with Co^{3+} on the Al1-site is shown in Figure 4 (b). As can be seen, the deviation between the experimental data and the fit is substantially larger than for Co on the Al3-site, resulting in an increase of the R-factor to 0.075. Furthermore, it was not possible to fit the data employing a single S_0^2 value for all the shells. In particular, while a global value for the Co−O, Co−Al single, and Co−Al−O multiple scattering paths of $S_0^2 = 0.78 \pm 0.19$ was determined, the S_0^2 for the Co−Ba shells had to be reduced to 0.53 ± 0.11. Furthermore, larger displacements of Ba-atoms from their regular lattice sites were necessary for fitting the experimental data, making the Al1-site in conclusion a less likely position for the Co-dopant. Besides, it should be mentioned that similar results were also obtained for EXAFS fits for Co on the Al2- and Al4-sites (not shown), so that the substitution of the Co dopant on the Al3 position within the $BaAl_2O_4$ lattice appears most likely due to EXAFS data presented here. By directing the spotlight onto the accurate determination of the Co^{3+}−O bond distances in tetrahedrally coordinated systems the ongoing research will consider (*i*) the refinement of PXRD data, and (*ii*) measurements and fitting of the EXAFS oscillation patterns to confirm the present results.

3.3. PXRD Characterization. The qualitative phase analysis by PXRD patterns collected at RT after thermal treatment of the pure $BaAl_2O_4$ and Co-doped $BaAl_2O_4$ precursors revealed that a completely single-phase was obtained (Figure 5), resembling that of the reported $BaAl_2O_4$[10]. Indexing of the powder patterns led to plausible hexagonal unit cell parameters and

the space group determination procedure confirmed the non-centrosymmetric $P6_3$. The formation of a polycrystalline Co-doped phase resulted in the change of unit cell dimensions, which was visible as a discrete shift of the diffraction peaks.
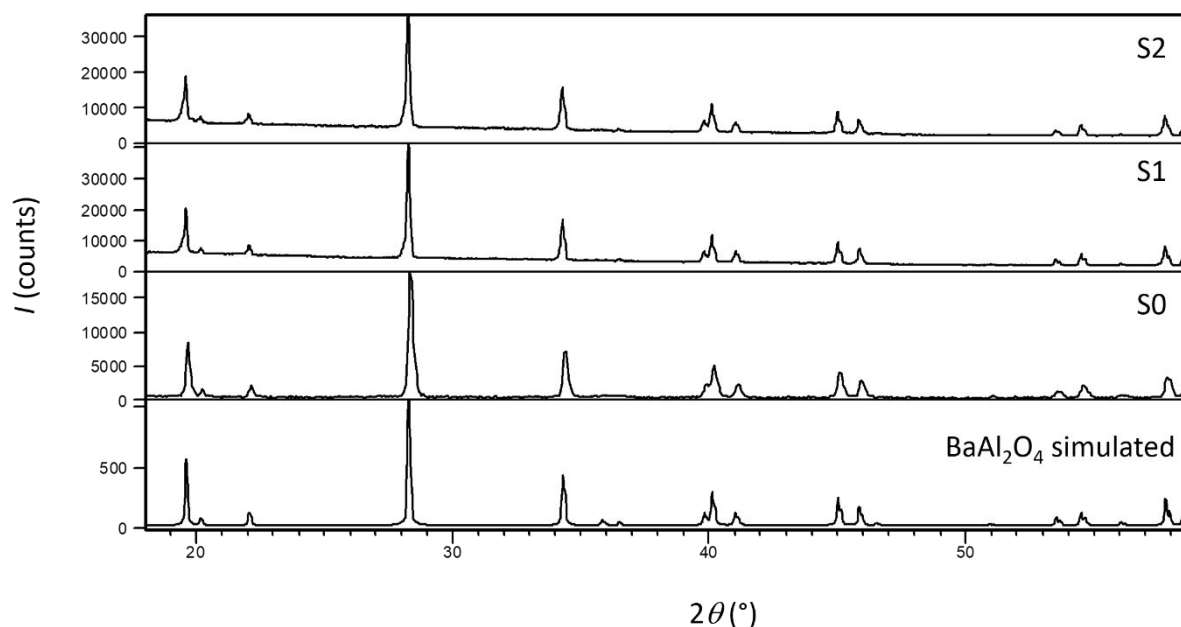
Figure 5. Laboratory PXRD data from samples S0–S2 (λ=1.5406 Å) at ambient temperature. The experimental data match the simulated PXRD pattern (bottom) of pure $BaAl_2O_4$ (ICSD card no. 75426; s. g. $P6_3$, a = 10.449(1) Å, and c = 8.793(1) Å)[10].

Refined unit-cell parameters a and c of pure $BaAl_2O_4$ (sample S0) and Co-doped $BaAl_2O_4$ (samples S1 and S2) are listed in Table 2 along with the Co content. The unit-cell parameter a slightly increased, parameter c slightly decreased, while unit-cell volume scarcely increased on the Co-doping. Considering the ionic radii for the four-coordinated Al^{3+} (0.39 Å)[86] and making use of the results from the XAS experiments one can decisively locate the positions of Co^{3+} dopants at the Al3 sites within the aluminate host. Accordingly, the initial Rietveld refinement of the structural model for the sample S0 demonstrated that the starting crystal structure quite nicely fits the one of the $BaAl_2O_4$ host and facilitates the comparison with previously published experimental results (ICSD card no. 75426)[10]. However, refinements of Al3 sites substituted

by Co^{3+} within the $BaAl_2O_4$ host lattice (samples S1 and S2) quickly revealed the occurrence of

noticeable changes in tetrahedral Al–O bond lengths. Final Rietveld refinements (Figure 6)

gave the sum formula $Ba(Al_{0.998}Co_{0.002})_2O_4$ (*i.e.* 0.77 at. % Co) and $Ba(Al_{0.991}Co_{0.009})_2O_4$ (*i.e.*

3.79 at. % Co) for samples S1 and S2, respectively. It should also be noted that the increase of

the unit cell volume for samples S0, S1, and S2 qualitatively mirrors the increasing amount of

Co^{3+} with a larger ionic radius in comparison to Al^{3+}. Thus the concentrations calculated from

the X-ray absorption data and the Rietveld refinements are in acceptable agreement.
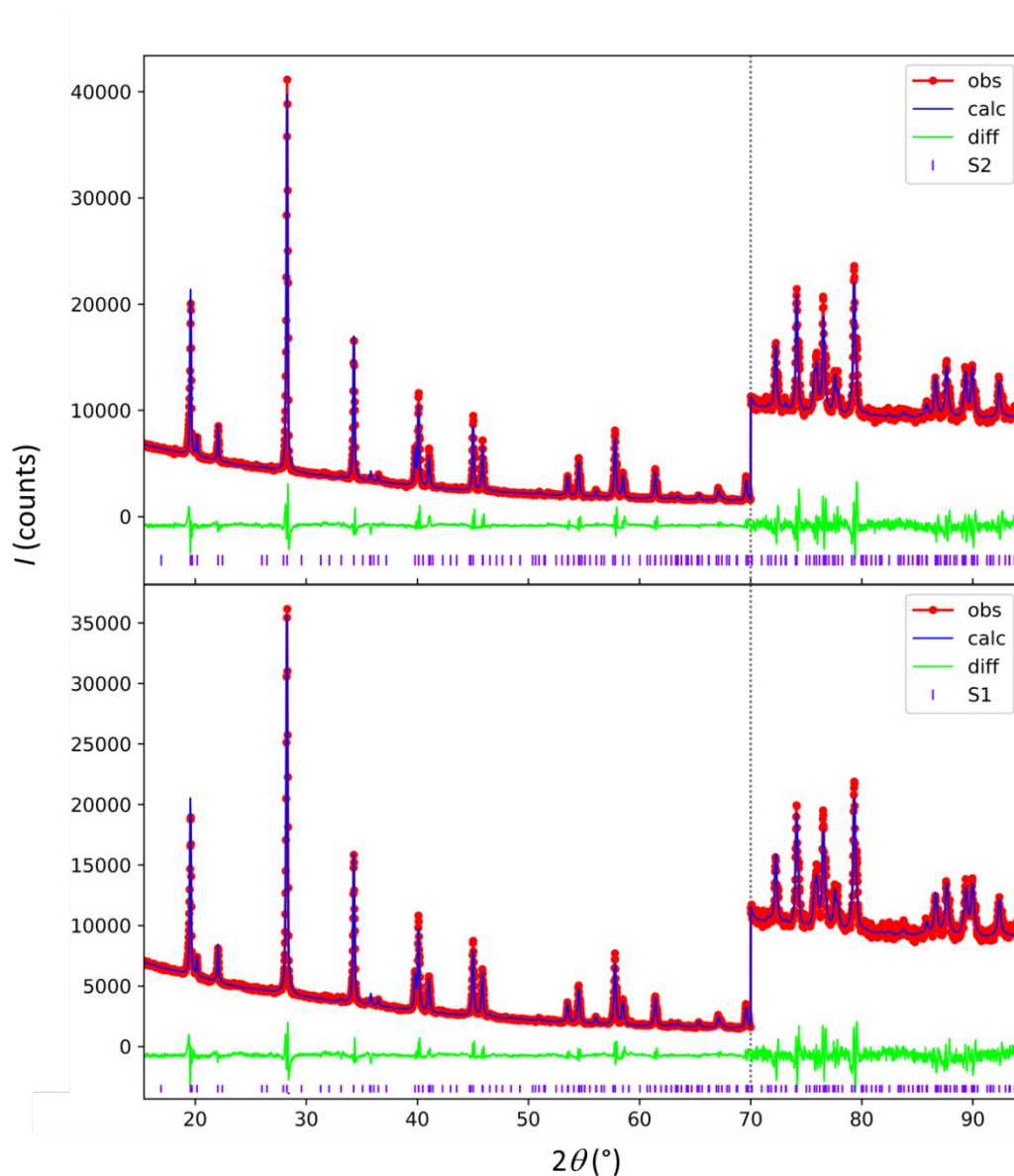
Figure 6. Final observed (red circles) and calculated (blue solid lines) powder diffraction

profiles for samples S1 and S2, respectively at 293 K as obtained from the Rietveld refinements

23

by PXRD data. The lower green solid lines show the difference profiles, whilst purple tick marks show the reflection positions. For clarity, the diffraction patterns are given magnified 7× from 70 to 100° 2θ.

Table 2. Summary of resulting structural parameters and reliability factors from Rietveld refinements of samples S0−S2 against PXRD data collected at RT.

sample	Co cont. (at. %)	unit cell parameters (Å) and V (Å³)	R_{wp} (%)	atom	x	y	z	s.o.f.	Wyck. position	site sym.	B_{iso} (Å²)
S0	0	a=10.4485(4)	5.52	Ba1	0.0000	0.0000	0.25	1	2a	3	0.54(2)
		c=8.7910(2)		Ba2	0.504(4)	0.0022(8)	0.258(5)	1	6c	1	0.54(2)
		V=831.14(5)		Al1	0.160(2)	0.336(3)	0.061(6)	1	6c	1	0.85(6)
				Al2	0.154(8)	0.340(7)	0.444(2)	1	6c	1	0.85(6)
				Al3	0.3333	0.6667	0.941(7)	1	2b	3	0.85(6)
				Al4	0.3333	0.6667	0.554(4)	1	2b	3	0.85(6)
				O1	0.182(2)	0.010(4)	0.987(3)	1	6c	1	0.95
				O2	0.674(8)	0.001(8)	0.03(5)	1	6c	1	0.95
				O3	0.492(6)	0.169(3)	0.996(4)	1	6c	1	0.95
				O4	0.185(7)	0.501(8)	0.000(4)	1	6c	1	0.95
				O5	0.118(5)	0.303(9)	0.252(7)	1	6c	1	0.95
				O6	0.3333	0.6667	0.749(1)	1	2b	3	0.95
S1	(0.77 ± 0.12)	a=10.4502(1)	5.58	Ba1	0.0000	0.0000	0.25	1	2a	3	0.60(4)
		c=8.7888(1)		Ba2	0.503(6)	0.0021(4)	0.258(4)	1	6c	1	0.60(4)
		V=831.21(1)		Al1	0.160(6)	0.337(4)	0.061(6)	1	6c	1	0.87(6)
				Al2	0.154(6)	0.341(5)	0.444(6)	1	6c	1	0.87(6)
				Al3	0.3333	0.6667	0.942(8)	0.996	2b	3	0.87(6)
				Co	0.3333	0.6667	0.942(8)	0.004	2b	3	0.87(6)
				Al4	0.3333	0.6667	0.554(7)	1	2b	3	0.87(6)
				O1	0.183(4)	0.010(5)	0.986(7)	1	6c	1	0.95
				O2	0.675(7)	0.001(7)	0.03(6)	1	6c	1	0.95
				O3	0.491(8)	0.169(8)	0.996(5)	1	6c	1	0.95
				O4	0.185(8)	0.503(7)	0.000(3)	1	6c	1	0.95
				O5	0.119(4)	0.303(5)	0.254(7)	1	6c	1	0.95
				O6	0.3333	0.6667	0.749(2)	1	2b	3	0.95
S2	(3.79 ± 0.83)	a=10.4519(1)	5.01	Ba1	0.0000	0.0000	0.25	1	2a	3	0.71(3)
		c=8.7871(1)		Ba2	0.503(5)	0.0021(9)	0.258(6)	1	6c	1	0.71(3)
		V=831.32(1)		Al1	0.160(6)	0.337(5)	0.062(6)	1	6c	1	0.92(7)
				Al2	0.154(8)	0.341(8)	0.444(9)	1	6c	1	0.92(7)
				Al3	0.3333	0.6667	0.942(9)	0.981	2b	3	0.92(7)
				Co	0.3333	0.6667	0.942(9)	0.019	2b	3	0.92(7)
				Al4	0.3333	0.6667	0.554(8)	1	2b	3	0.92(7)
				O1	0.183(5)	0.010(8)	0.987(3)	1	6c	1	0.95
				O2	0.677(2)	0.002(5)	0.02(6)	1	6c	1	0.95
				O3	0.491(7)	0.171(6)	0.997(4)	1	6c	1	0.95
				O4	0.185(9)	0.504(9)	0.000(4)	1	6c	1	0.95
				O5	0.120(7)	0.304(8)	0.254(5)	1	6c	1	0.95
				O6	0.3333	0.6667	0.747(4)	1	2b	3	0.95

Table 3. Molecular geometry refinement details of samples S0−S2 from Rietveld refinement against PXRD data collected at RT.

| sample	molecular dimensions (Å, °)						
S0	Ba−O1×3	2.97(2)	Ba2−O2	2.69(3)	Al1−O1	1.81(4)	Al2−O1	1.71(5)
	−O1×3	2.80(4)	−O2	3.00(4)	−O2	1.83(5)	−O2	1.76(3)
	−O5×3	2.77(3)	−O3	2.93(3)	−O4	1.73(4)	−O3	1.77(6)
	average	2.85(3)	−O3	2.76(4)	−O5	1.72(8)	−O5	1.72(4)
			−O4	2.80(3)	average	1.77(8)	average	1.74(6)
			−O4	2.93(5)				
			−O5	2.92(5)				
			−O5	3.44(4)				
			−O6	2.97(3)	Al3−O4×3	1.72(8)	Al4−O3×3	1.83(7)
			average	2.95(4)	−O6	1.70(8)	−O6	1.73(6)
					average	1.72(8)	average	1.80(7)
	Al1−O5−Al2	156.3(6)						
	Al3−O6−Al4	179.9(4)						
S1	Ba−O1×3	2.77(3)	Ba2−O2	2.69(6)	Al1−O1	1.81(7)	Al2−O1	1.71(5)
	−O1×3	2.97(3)	−O2	3.01(6)	−O2	1.83(6)	−O2	1.72(8)
	−O5×3	2.80(2)	−O3	2.93(4)	−O4	1.73(9)	−O3	1.76(8)
	average	2.84(3)	−O3	2.76(3)	−O5	1.72(6)	−O5	1.72(7)
			−O4	2.80(4)	average	1.77(7)	average	1.73(7)
			−O4	2.97(7)				
			−O5	2.92(4)				
			−O5	3.43(3)				
			−O6	2.99(6)	Al3/Co−O4×3	1.74(8)	Al4−O3×3	1.82(6)
			average	2.94(5)	−O6	1.71(9)	−O6	1.73(7)
					average	1.73(9)	average	1.80(7)
	Al1−O5−Al2	156.1(2)						
	Al3−O6−Al4	179.6(4)						
S2	Ba−O1×3	2.80(7)	Ba2−O2	2.70(3)	Al1−O1	1.81(6)	Al2−O1	1.70(3)
	−O1×3	2.97(6)	−O2	3.02(5)	−O2	1.84(7)	−O2	1.74(7)
	−O5×3	2.76(4)	−O3	2.94(5)	−O4	1.70(9)	−O3	1.78(5)
	average	2.84(6)	−O3	2.76(6)	−O5	1.75(6)	−O5	1.71(3)
			−O4	2.81(7)	average	1.76(7)	average	1.73(5)
			−O4	2.99(7)				
			−O5	2.91(8)				
			−O5	3.43(4)				
			−O6	2.98(5)	Al3/Co−O4×3	1.75(8)	Al4−O3×3	1.84(7)
			average	2.95(6)	−O6	1.73(9)	−O6	1.73(4)
					average	1.74(9)	average	1.79(6)
	Al1−O5−Al2	156.1(9)						
	Al3−O6−Al4	179.3(8)						

A selection of refined metal-oxygen distances along with the values of Al1−O5−Al2 and Al3−O6−Al4 angles in the structure of the samples S1 and S2 are listed in Table 3. The

substitution of Al^{3+} cations by Co^{3+} at Al3 sites led to an increase of the average tetrahedral

bond lengths from 1.72(8) in sample S0 to 1.74(9) in sample S2. Cobalt substitution

simultaneously induced a slight decrease in average tetrahedral symmetries around Al1 sites

from 1.77(8) in sample S0 to 1.76(7) in sample S2. The average distances in $(Al2)O_4$, and

$(Al4)O_4$ tetrahedra as well as the bond lengths in $(Ba1)O_9$ and $(Ba2)O_9$ coordination tend to

remain constant within the standard deviation. It is important to note that the $Co^{3+}-O$ distance

obtained from EXAFS fits of sample S1 has a value of 1.92 ± 0.01 Å, which is substantially

larger compared to that of the Al/Co$-$O bond of the Rietveld refinements with values of ca.

1.72 Å for sample S0, 1.73 Å for S1, and 1.74 Å for S2. Inspecting those obvious differences,

one has to keep in mind that a Rietveld refinement yields the average bond distance of all

equivalent lattice sites, here, in particular, the $2b$ position (see Table 2), irrespective of whether

they are occupied by an Al^{3+} or a Co^{3+} ion. For EXAFS experiments, however, the Co$-$O bonds

can be studied separately due to the element-specific nature of the method. The larger Co$-$O

bond distance derived from EXAFS thus reflects the different local geometry around Co and

Al, which is closely related to the substantially different ionic radii of the two cations. If the

site occupancies by Al and Co are considered in the calculation of average bond lengths, the

results obtained by PXRD and EXAFS agree quantitatively well as follows: ideal $BaAl_2O_4$

features equal numbers of Al1, Al2, Al3, and Al4 sites, and assuming that all of the substituted

Co is located on Al3 positions, the concentration of Co on $2b$-sites is four times larger than the

total amount of Co, implying about $0.8 \times 4 = 3.2$ % for sample S1 and $3.7 \times 4 = 14.8$ % for

sample S2. Considering the original bond length of Al3$-$O to be 1.72 Å for 96 % of the Al3 $2b$

lattice sites and 4 % with 1.92 Å for the Co-occupied $2b$ positions would result in a median of

1.73 Å for sample S1, and accordingly, $85\ \% \times 1.72$ Å plus $15\ \% \times 1.92$ Å would result in about

1.75 Å for sample S2, respectively. Those average bond lengths are in quantitative agreement

with the results of the Rietveld refinements. Calculated microstructural parameters, induced by

the Co^{3+} dopant tended to increase with the doping level. In particular, the lattice strains increased from 0.02(1) % in sample S0 to 0.14(1) % in sample S2, while the values of the crystallite sizes obtained from the line-broadening analysis performed during the structure refinements increased significantly, from 56.7(1) nm in sample S0 to 94.5(1) nm and 126.41(1) nm in samples S1 and S2, respectively.

3.4. Magnetization Viewpoints. The results of magnetic measurements of polycrystalline samples are shown in Figure 7. The $\chi \cdot T(T)$ dependence for all samples looks quite similar: in the ~50–298 K range the $\chi \cdot T$ values remain almost constant (sample S0) or slightly decrease (samples S1 and S2) with decreasing the temperature, and as the temperature is lowered below ~50 K they decrease considerably with cooling down to 2 K. The broad peak around 50 K indicates the presence of oxygen. Namely, the great affinity of pure $BaAl_2O_4$ for oxygen is firmly established by our group demonstrating the material's extraordinary magnetic response at temperatures below ~60 K.[9] The magnetic states of Co^{3+}-doped samples discussed in this study are expected to give rise to a paramagnetic contribution in the magnetization signal due to the small amount of magnetic Co^{3+} substituted within the diamagnetic $BaAl_2O_4$ matrix. However, the trend of the magnetic response below ~30 K showing the considerable decrease of effective magnetic moment with cooling down further implies that measurements cannot be modeled by the Curie law, thus demanding that some form of the spin-orbit coupling (*i.e.* microscopic anisotropy) should be introduced into the analysis. Before the analysis of magnetic measurements, the values of magnetization for the pure $BaAl_2O_4$ (sample S0) were carefully subtracted from the magnetization of samples S1 and S2 to approach the magnetization of bare magnetic Co ions with the best approximation. However, the oxygen signal couldn't be substracted ideally to get the pure cobalt signal, possibly because not only the amount of oxygen is different in different samples, but also the form in which oxygen is present in samples can differ. That could very well be the reason why the oxygen peak is shifted towards lower values

in sample S1 (~30 K). Consequently, it was necessary to discard some data in a fitting procedure

where oxygen contamination is significant (12–45 K in sample S1, and 30–70 K in sample S2).
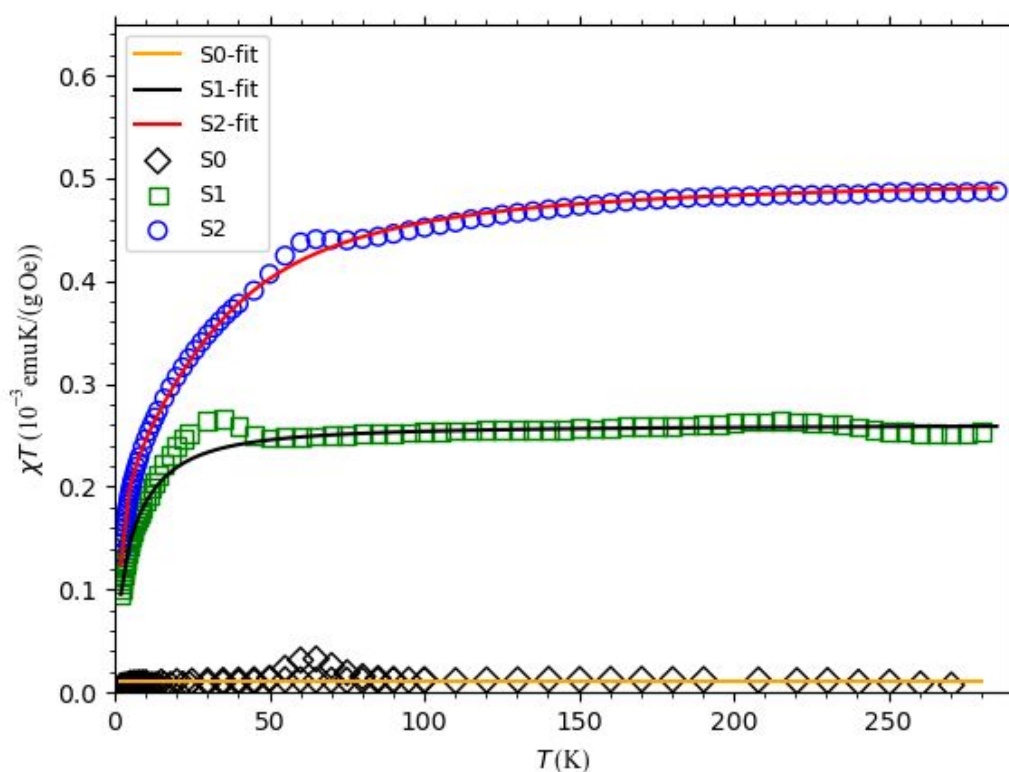
Figure 7. Temperature dependencies of the $\chi \cdot T$ product for samples S0–S2 measured in 1000

Oe. Obtained fits for samples S0, S1, and S2 are depicted by orange, black and red lines,
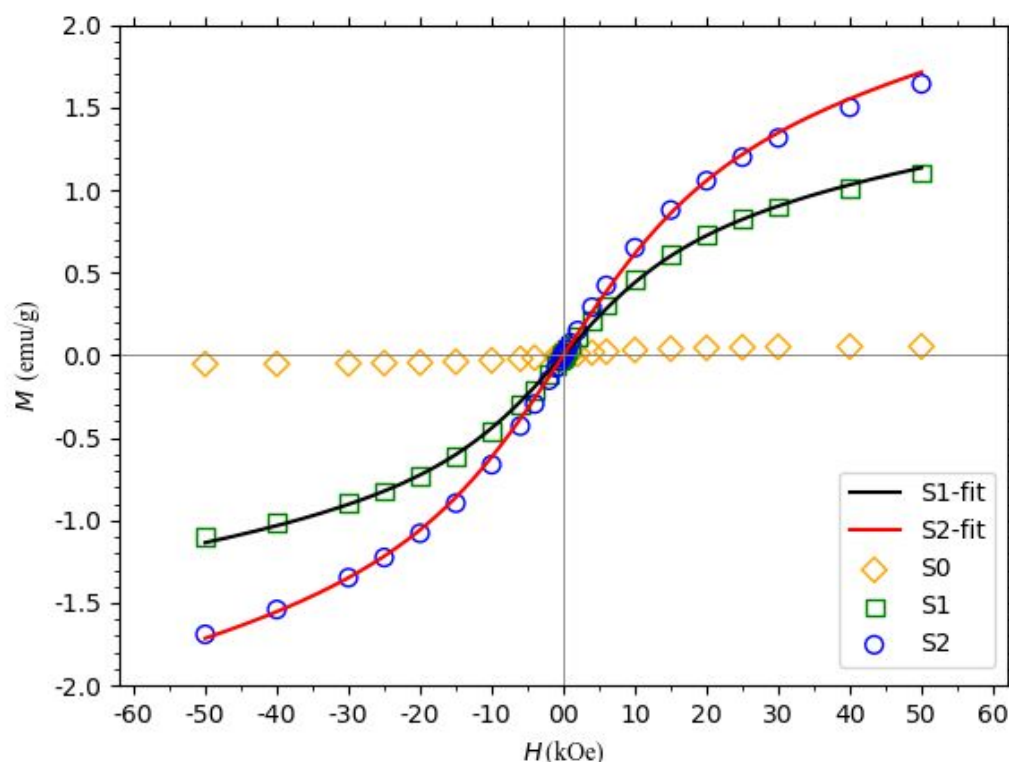
respectively.

It has also to be noted, that no fit was satisfactory on magnetization data when the half-integer

values of the spin were assumed, due to significantly different behavior of $\chi \cdot T(T)$ curves at low

temperatures. Also, the results for the ratios of Co to Ba cations using $S=1$ did not comply with

the XAS results. In conclusion, the spin state of Co ions $S=2$ agreed much better with the above

findings. Obtained fits of $\chi \cdot T(T)$ dependences for the Co^{3+}-doped samples using the

Hamiltonian (1) with $S=2$ are shown in Figure 7. The fitting curves were obtained by

minimization of relative error between measured $\chi \cdot T$ and numerically calculated data from

diagonalization of the Hamiltonian in terms of rhombic and axial ZFS parameters D and E, Co

28

percentage x, and g-factors. The corresponding optimal-fit parameters for the samples S1 and S2, and their estimated errors, are presented in Table 4.

Table 4. Spin-Hamiltonian parameters for samples S1 and S2 obtained from the fitting of magnetic data.

sample	D (K)	E (K)	x (%)	g_x	g_y	g_z
S1	10.8(0.5)	2.7(0.3)	0.92(0.19)	2.34(0.21)	1.79(0.16)	2.42(0.22)
S2	26.3(1.0)	10.4(0.8)	1.77(0.33)	2.52(0.25)	1.70(0.15)	2.30(0.22)

Using the optimal fitting parameters of $\chi \cdot T(T)$ curves we also plotted the calculated $M(H)$ curves over the measured data (Figure 8). Good agreement is observed confirming the consistency of the obtained parameters. The high relative uncertainty of g-tensor components and Co percentage stems from the inability to determine both of those physical quantities simultaneously from magnetic measurements alone. However, we expect the mean quadratic value of g somewhere between 2.0–2.4 according to literature, and in our case, 2.20 is used to obtain the most probable range of values for Co percentages (Table 4). The value of x for S1 is in good agreement with XANES/XAS measurements, while for S2 there is a larger deviation, which only partially can be understood within a difference of the g-factors that can vary between 2.0 and 2.4. Though there are other factors involved, the reasons for such deviations are not explored yet.

Figure 8. The *M(H)* measurements for samples S0−S2 and curves plotted using optimal fitting

parameters for the *χ·T(T)* curves.

Obtained values of second-order axial and rhombic ZFS parameters, *D* and *E*, respectively, are

of the order of magnitude which is in good agreement with literature data for tetrahedrally

coordinated Co^{3+} ion[76] considering that those values vary considerably with the degree of local

distortion. The increase of *D* and *E* with an increase of *x* corroborates the fact that the strain

induced by the radius difference between Co^{3+} and Al^{3+} increases with increasing substitution

of Co, leading to an increasing distortion of angles and distances around the cobalt ions if

compared with the ideal positions in $BaAl_2O_4$ host (see Tables 1-3). All results show that Co-

substitution cannot be performed with a high percentage, and it could be the reason that

magnetic analysis gives a somewhat lower *x* than the highest confirmed in the XAS experiment,

due to the increased stress and distortion. Our modeling gives reliable result for all parameters

for lower *x*, however, when *x* increases, much more distortions in the crystal lattice and

nonideally random distribution of substituents, makes the model further from the ideal situation, and deviations between different techniques are understandable. The obtained axial zero-field splitting parameter D is within the values reported by Saber and Dunbar[87]. For comparison, the tetrahedrally coordinated Co^{3+} can have such or even larger anisotropy, with different possibilities for a spin (0, 2, or even 1), and with anisotropic g-factor from 2.0 to 2.4.[88] Nonetheless, our results fit very well into sparsely known data about the controversially discussed Co^{3+} coordination[89,90]. Although more advanced microscopic magnetic properties cannot be studied in our substituted bulk material using DC magnetization, this is a clear example that besides the axial anisotropy D, also the transversal component E should be taken into account to get a reliable model. The success of the model based on the spin Hamiltonian (1) confirms the tetrahedral position of Co^{3+}, as established also in EXAFS modeling since octahedral coordination would produce considerably different $M(T)$ dependence and need for different model Hamiltonian. Also, the XANES calculations support the presence of distorted tetrahedral oxygen coordination around Co^{3+}, in the case of an ideal tetrahedron, a much stronger pre-peak would have been observed in the XANES at about 7708 eV, while in the case of octahedral coordination, the pre-peak position would be different, as well as the EXAFS data would have suggested a larger number of nearest oxygen neighbors of $N \approx 6$ in the first coordination shell. Moreover, it is concluded that D and E increase with an increased amount of substituent ion, which is due to stronger distortions of the host lattice with the introduction of additional bigger ions.

4. CONCLUSIONS

This work presents the study of the effects of Co^{3+} dopant on the chemical environment and magnetic properties within the $BaAl_2O_4$ lattice. Compelling evidence for the symmetry of the coordination site, oxidation state, and concentration of dopant cations has been provided by

detecting the fluorescence radiation during XANES measurements at the Co K-edge of $BaAl_2O_4$ host crystal doped with 0.77 and 3.79 at. % Co. The coordination numbers and bond distances of successive shells around the absorbing Co^{3+} dopant were extracted from the EXAFS oscillation patterns. The XAS results confirm that Co^{3+} ions preferentially replace aluminum in tetrahedral Al3 sites within the $BaAl_2O_4$ host lattice. A unique and quite rarely documented tetrahedral geometry around Co^{3+} was further complemented with the diffraction studies. Rietveld refinement procedures established that Co^{3+}-doped $BaAl_2O_4$ is isostructural with $BaAl_2O_4$ however, with an important difference: the Co^{3+} dopant located at Al3 sites simultaneously induces an increase of the average distances in $(Al3)O_4$ coordinations. A comparative magneto-structural analysis clearly shows that the subtle modifications of $BaAl_2O_4$ crystal lattice by Co^{3+} also give rise to the axial and rhombic ZFS terms, leading to larger anisotropy, with most probable spin 2.

Conflicts of interest

There are no conflicts to declare.

ACKNOWLEDGEMENTS

ASSOCIATED CONTENT

Supporting Infromation

Details on XANES and FEFF–XANES calculation data.

AUTHOR INFORMATION

Corresponding Author

*Martina Vrankić, e-mail: Martina.Vrankic@irb.hr

REFERENCES

(1) Burda, C.; Chen, X.; Narayanan, R., El-Sayed, M.A. Chemistry and properties of nanocrystals of different shapes. *Chem. Rev.* **2005**, *105*, 1025–1102.

(2) Kamat, P.V. Photochemistry on nonreactive and reactive (semiconductor) surfaces. *Chem. Rev.* **1993**, *93*, 267–300.

(3) Jiang, J.; Zhao, K.; Xiao, X.; Zhang L. Synthesis and facet-dependent photoreactivity of BiOCl single-crystalline nanosheets. *J. Am. Chem. Soc.* **2012**, *134*, 4473–4476.

(4) Ishii, Y.; Tsukasaki, H.; Tanaka, E.; Kawaguchi, S.; Mori, S. Emergence of a fluctuating state in the stuffed tridymite-type oxides $Ba_{1-x}Sr_xAl_2O_4$. *Phys. Rev. B*, **2016**, *94*, 184106.

(5) Brito, H.F.; Felinto, M.C.F.C.; Hölsä, J.; Laamanen, T.; Lastusaari, M.; Malkamäki, M.; Novák, P.; Rodrigues, L.C.V.; Stefani, R. DFT and synchrotron radiation study of Eu^{2+} doped $BaAl_2O_4$. *Opt. Mater. Express,* **2012**, *2*, 420–43.

(6) Li, X.; Budai, J.D.; Liu, F.; Howe, J.Y.; Zhang, J.; Wang, X.-J.; Gu, Z.; Sun, C.; Meltzer, R.S.; Pan, Z. New yellow $Ba_{0.93}Eu_{0.07}Al_2O_4$ phosphor for warm-white light-emitting diodes through single-emitting-center conversion. *Light: Science & Applications* **2013**, *2*, e50.

(7) Hyland, R.W.Jr.; Quintenz, J.P.; Dunville, B.T.; Subrahmanyam, G.U.S. Patent 6969475 B2, **2005**.

(8) Kim, C.-H; Kwon, I.-E.; Park, H.-H.; Hwang, Y.-J.; Bae, H.-S.; Yu, B.-Y.; Pyun, C.-H.; Hong, G.-Y. Phosphors for plasma display panels. *J. Alloys Compd.* **2000**, *311*, 33−39.

(9) Vrankić, M.; Šarić, A.; Bosnar, S.; Pajić, D.; Dragović, J.; Altomare, A.; Falcicchio, A.; Popović, J.; Jurić, M.; Petravić, M.; Jelovica Badovinac, I.; Dražić, G.; Magnetic oxygen stored in quasi-1D form within $BaAl_2O_4$ lattice. *Sci. Rep.* **2019**, *9*, 15158.

(10) Huang, S.-Y.; von der Mühll, R.; Ravez, J.; Chaminade, J.P.; Hagenmüller, P.; Couzi, M.J. Structural, ferroelectric and pyroelectric properties of nonstoichiometric ceramics based on $BaAl_2O_4$. *Solid State Chem.* **1994**, *109*, 97−105.

(11) Vrankić, M., Gržeta, B., Lützenkirchen-Hecht, D., Bosnar, S.; Šarić, A. Chromium environment within Cr-doped $BaAl_2O_4$: correlation of X-ray diffraction and X-ray absorption spectroscopy investigations. *Inorg. Chem.* **2015**, *54*, 11127–11135.

(12) Gržeta, B.; Lützenkirchen-Hecht, D.; Vrankić, M.; Bosnar, S.; Šarić, A.; Takahashi, M.; Petrov, D.; Bišćan, M.; Environment of the Eu^{3+} ion within nanocrystalline Eu-doped $BaAl_2O_4$: correlation of X‑ray diffraction, Mössbauer spectroscopy, X‑ray absorption spectroscopy, and photoluminescence investigations. *Inorg. Chem.* **2018**, *57*, 1744−1756.

(13) Lou, Z.; Hao, J.; Cocivera, M. Luminescence studies of $BaAl_2O_4$ films doped with Tm, Tb, and Eu. *J. Phys. D: Appl. Phys.* **2002**, *35*, 2841−2845.

(14) Singh, V.; Natarajan, V.; Zhu, J.-J. Studies on Eu doped Ba and Zn aluminate phosphors prepared by combustion synthesis. *Opt. Mater.* **2007,** *29*, 1447−1451.

34

(15) Peng, M.; Hong, G. Reduction from Eu^{3+} to Eu^{2+} in $BaAl_2O_4$:Eu phosphor prepared in an oxidizing atmosphere and luminescent properties of $BaAl_2O_4$:Eu. *J. Lumin.* **2007**, *127*, 735−740.

(16) Singh, V.; Chakradhar, R. P. S.; Rao, J. L.; Zhu, J.-J. Studies on red-emitting Cr^{3+} doped barium aluminate phosphor obtained by combustion process. *Mater. Chem. Phys.* **2008**, *111*, 143−148.

(17) Zhang, L.-W.; Wang, Li.; Zhu, Y.-F. Synthesis and performance of $BaAl_2O_4$ with a wide spectral range. *Adv. Funct. Mater.* **2007**, *17*, 3781–3790.

(18) S. Rezende, M.V.dos; Valerio, M.E.G.; Jackson, R.A. Computer modelling of the reduction of rare earth dopants in barium aluminate. *J. Solid State Chem.* **2011**, *184*, 1903–1908.

(19) S. Rezende, M.V.dos; Valerio, M.E.G.; Jackson, R.A. Study of $Eu^{3+} \rightarrow Eu^{2+}$ reduction in $BaAl_2O_4$:Eu prepared in different gas atmospheres. *Mater. Res. Bull.* **2014**, *61*, 348–351.

(20) Deb, S.K. Optical and photoelectric properties and colour centres in thin films of tungsten oxide. *Philos. Mag.* **1973**, *27*, 801–822.

(21) Henderson, B. Anion vacancy centers in alkaline earth oxides. *Crit. Rev. Solid State Mater. Sci.* **1980**, *9*, 1–60.

(22) Stoneham, A. M. Theory of defects in solids: electronic structure of defects in insulators and semiconductors. Oxford University Press, Oxford, **2001**.

(23) Samson, S.; Fonstad, C.G. Defect structure and electronic donor levels in stannic oxide crystals. *J. Appl. Phys.* **1973**, *44*, 4618– 4621.

(24) Frank, G.; Kostlin, H. Electrical properties and defect model of tin-doped indium oxide layers. *Appl. Phys. A* **1982**, *27*, 197–206.

35

(25) Williams, D.E. Semiconducting oxides as gas-sensitive resistors. *Sens. Actuators, B* **1999**, *57*, 1–16.

(26) Lany, S.; Zunger, A. Dopability, intrinsic conductivity, and nonstoichiometry of transparent conducting oxides. *Phys. Rev. Lett.* **2007**, *98*, 045501.

(27) Agoston, P.; Albe, K.; Nieminen, R.M.; Puska, M.J. Intrinsic n-type behavior in transparent conducting oxides: A comparative hybrid-functional study of In_2O_3, SnO_2, and ZnO. *Phys. Rev. Lett.* **2009**, *103*, 245501.

(28) Xiong, K.; Robertson, J.; Gibson, M.C.; Clark, S.J. Defect energy levels in HfO_2 high-dielectric-constant gate oxide. *Appl. Phys. Lett.* **2005**, *87*, 183505.

(29) Broqvist, P.; Pasquarello, A. Oxygen vacancy in monoclinic HfO_2: A consistent interpretation of trap assisted conduction, direct electron injection, and optical absorption experiments. *Appl. Phys. Lett*. **2006**, *89*, 262904.

(30) Gavartin, J.L.; Munoz Ramo, D.; Shluger, A.L.; Bersuker, G.; Lee, B.H. Negative oxygen vacancies in HfO_2 as charge traps in high-*k* stacks. *Appl. Phys. Lett.* **2006**, *89*, 082908.

(31) Tse, K.; Liu, D.; Xiong, K.; Robertson, J. Oxygen vacancies in high-k oxides. *Microelectron. Eng.* **2007**, *84*, 2028–2031.

(32) Vanheusden, K.; Warren, W.L.; Seager, C.H.; Tallant, D.R.; Voigt, J.A.; Gnade, B.E. Mechanisms behind green photoluminescence in ZnO phosphor powders. *J. Appl. Phys.* **1996**, *79*, 7983.

(33) Xie, T.-H.; Lin, J. Origin of Photocatalytic deactivation of TiO_2 film coated on ceramic substrate. *J. Phys. Chem. C* **2007**, *111*, 9968–9974.

(34) Wang, J.; Tafen, D.N.; Lewis, J.P.; Hong, Z.; Manivannan, A.; Zhi, M.; Li, M.; Wu, N. Origin of photocatalytic activity of nitrogen-doped TiO_2 nanobelts, *J. Am. Chem. Soc.* **2009**, *131*, 12290–12297.

36

(35) Rezende, S.M.V. dos; Montes P.J.R; Andrade, A.B.; Macedo Z.S.; Valerio, M.E.G. Mechanism of X-ray excited optical luminescence (XEOL) in europium doped $BaAl_2O_4$ phosphor. *Phys. Chem. Chem. Phys.*, **2016**, *18*, 17646–17654.

(36) Nagai, T.; Yamada, Y.; Tanabe, K.; Terasaki, I.; Taniguchi, H. Photo-induced persistent enhancement of dielectric permittivity in $Zn:BaAl_2O_4$. *Appl. Phys. Lett*. **2017**, *111*, 232902.

(37) Sakai, R.; Katsumata, T.; Komuro, S.; Morikawa, T. Effect of composition on the phosphorescence from $BaAl_2O_4$: Eu^{2+}, Dy^{3+} crystals. *J. Lumin.* **1999**, *85*, 149–154.

(38) Lin, Y.H.; Zhang, Z.T.; Tang, Z.L.; Zhang, J.Y.; Zheng, Z.S.; Lu, X. The characterization and mechanism of long afterglow in alkaline earth aluminates phosphors co-doped by Eu_2O_3 and Dy_2O_3. *Mater. Chem. Phys.* **2001**, *70*, 156–159.

(39) Rodrigues L.C.V.; Carvalho, C.A.A.; Felinto, M.C.F.C.; Lastusaari, M.; Hölsä, J. Persistent luminescence of Eu^{2+} and Dy^{3+} doped barium aluminate ($BaAl_2O_4:Eu^{2+}$, Dy^{3+}) materials. *Opt. Mater.* **2009**, *31*, 1815–1818.

(40) Ayvacikli, M. Characterization of a green-emitting copper doped barium aluminate phosphor. *Spectrosc. Lett.*, **2014**, *47*, 504–511.

(41) Li, J.; Lan X.-K.; Du K.; Song X.-Q.; Lu, W.-Z.; Fan, G.-F.; Lei, W. Crystal structures, dielectric properties and ferroelectricity in stuffed tridymite-type $BaAl_{(2-2x)}(Zn_{0.5}Si_{0.5})_{2x}O_4$ solid solutions. *Dalton Trans.*, **2019**, *48*, 3625–3634.

(42) Pan, M.-J.; Randall, C. A. A brief introduction to ceramic capacitors. *IEEE Electr. Insul. Magz.*, **2010**, *26*, 44–50.

(43) Hong, K.; Lee, T.H.; Suh, J.M.; Yoon, S.-H.; Jang, H.W. Perspectives and challenges in multilayer ceramic capacitors for next generation electronics. *J. Mater. Chem. C*, **2019**, *7*, 9782–9802.

(44) Li, J.; Lan, X.-K.; Du, K.; Song X.-Q.; Lu, W.-Z.; Fan, G.-F. Crystal structure and temperature dependence of permittivity in barium aluminate based solid solutions. *J. Am. Ceram. Soc.* **2019**, *00*, 1–11.

(45) Li, J.; Lan, X.-K.; Du, K.; Song, X.-Q.; Lu, W.-Z.; Wang, X.-H.; Lei, W. Ultrabroad temperature stability of stuffed tridymite-type $BaAl_2O_4$ co-doped by $[Zn_{0.5}Ti_{0.5}]^{3+}$ with weak ferroelectricity. *Ceram. Int.* **2019**, *45*, 22493–22497.

(46) Azough, F.; Al-Saffar, R.; Freer, R. A transmission electron microscope study of commercial X7R-type multilayer ceramic capacitors, *J. Am. Ceram. Soc.* **1998**, *18,* 75l–758.

(47) Wang, X.; Chen, R.; Zhilun, G.; Li, L. Temperature-stable dielectric ceramic composition for multilayer ceramic capacitors with base metal electrodes. U.S. Patent 7022635 B2, April 4, **2006**.

(48) Wang, X.; Tian, Z.; Tian, W.; Li, L. Nan complex oxide doped dielectric ceramic material preparation method thereof and multilayer ceramic capacitors made from the same. U.S. Patent 2009/0135546 A1, May 28, **2009**.

(49) Barber, Jr., F.; Karam, E.E.; Dunaway, R.; Rogers, R.L. Multilayer ceramic capacitors. U.S. Patent 4,435,738, March 6, **1984**.

(50) Hoshina, T.; Wada, S.; Kuroiwa, Y.; Tsurumi, T. Composite structure and size effect of barium titanate nanoparticles. *Appl. Phys. Lett.*, **2008,** *93*, 192914.

(51) Yan, T.; Shen, Z.-G.; Zhang, W.-W.; Chen, J.-F. Size dependence on the ferroelectric transition of nanosized $BaTiO_3$ particles. *Mater. Chem. Phys.*, **2006**, *98*, 450–455.

(52) Ishikawa, K; Uemori, T. Surface relaxation in ferroelectric perovskites. *Phys. Rev. B*, **1999**, *60*, 11841–11845.

(53) Luan, C.N.; Ma, J.; Zhu, Z.; Kong, L.Y.; Yu, Q.Q. Sol-gel synthesis and characterization of $BaAl_2O_4$ and $Co:BaAl_2O_4$ nanoparticles. *Adv. Mater. Res.* **2011**,*148/149*, 1067–1070.

(54) Takada, K.; Sakurai, H.; Takayama-Muromachi, E.; Izumi, F.; Dilanian, R.A.; Sasaki, T. A New superconducting phase of sodium cobalt oxide. *Adv. Mater,* **2004**, *16*, 1901−1905.

(55) Terasaki, I.; Sasago, Y.; Uchinokura, K. Large thermoelectric power in $NaCo_2O_4$ single crystals. *Phys. Rev. B,* **1997**, *56*, R12685−R12687.

(56) Belik, A.A.; Iikubo, S.; Kodama, K.; Igawa, N.; Shamoto, S.; Niitaka, S.; Azuma, M.; Shimakawa, Y.; Takano, M.; Izumi, F.; Takayama-Muromachi, E. Neutron powder diffraction study on the crystal and magnetic structures of $BiCoO_3$. *Chem. Mater.* **2006**, *18*, 798−803.

(57) Tsubouchi, S.; Kyômen, T.; Itoh, M.; Ganguly, P.; Oguni, M.; Shimojo, Y.; Morii, Y.; Ishii, Y. Simultaneous metal-insulator and spin-state transitions in $Pr_{0.5}Ca_{0.5}CoO_3$. *Phys. Rev. B* **2002**, *66*, 052418.

(58) Chen, J.M.; Chin, Y.Y.; Valldor, M.; Hu, Z. W.; Lee, J.M.; Haw, S.C.; Hiraoka, N.; Ishii, H.; Pao, C.W.; Tsuei, K.D.; Lee, J.F.; Lin, H.J.; Jang, L.Y.; Tanaka, A.; Chen, C.T.; Tjeng, L.H.A Complete High-to-Low spin state transition of trivalent cobalt ion in octahedral symmetry in $SrCo_{0.5}Ru_{0.5}O_{3-\delta}$. *J. Am. Chem. Soc.* **2014**, *136*, 1514–1519.

(59) Goodenough, J.B.; Raccah, P.M. Complex vs band formation in perovskite oxides. *J. Appl. Phys.* **1965**, *36*, 1031–1032.

(60) Haverkort, M.W.; Hu, Z.; Cezar, J.C.; Burnus, T.; Hartmann, H.; Reuther, M.; Zobel, C.; Lorenz, T.; Tanaka, A.; Brookes, N.B.; Hsieh, H.H.; Lin, H.-J.; Chen, C.T.; Tjeng, L.H. Spin state transition in $LaCoO_3$ studied using soft X-ray absorption spectroscopy and magnetic circular dichroism. *Phys. Rev. Lett.* **2006**, *97*, 176405.

(61) Oku, M. X-ray photoelectron spectrum of low-spin Co(III) in $LiCoO_2$. *J. Solid State Chem.* **1978**, *23*, 177−185.

(62) Hu, Z.; Mazumdar, C.; Kaindl, G.; de Groot, F.M.F.; Warda, S. Reinen, D. Valence electron distribution in $La_2Li_{1/2}Cu_{1/2}O_4$, $Nd_2Li_{1/2}Ni_{1/2}O_4$, and $La_2Li_{1/2}Co_{1/2}O_4$. *Chem. Phys. Lett.* **1998**, *297*, 321−328.

(63) Yamaura, K.; Zandbergen, H.W.; Abe, K.; Cava, R.J. Synthesis and properties of the structurally one-dimensional cobalt oxide $Ba_{1-x}Sr_xCoO_3$ ($0 \leq x \leq 0.5$). *J. Solid State Chem.* **1999**, *146*, 96−102.

(64) Martin, C.; Maignan, A.; Pelloquin, D.; Nguyen, N.; Raveau, B. Magnetoresistance in the oxygen deficient $LnBaCo_2O_{5.4}$ (Ln=Eu, Gd) phases. *Appl. Phys. Lett.* **1997**, *71,* 1421−1423.

(65) Lützenkirchen-Hecht, D.; Wagner, R.; Szillat, S.; Hüsecken, A.K.; Istomin, K.; Pietsch, U.; Frahm. R. The multi-purpose hard X-ray beamline BL10 at the DELTA storage ring. *J. Synchrotron Rad.* **2014**, *21*, 819–826.

(66) Zabinsky, S.I.; Rehr, J.J.; Ankudinov, A.; Albers, R.C.; Eller, M.J. Multiple-scattering calculations of x-ray-absorption spectra. *Phys. Rev. B*, **1995**, *52(4),* 2995−3009.

(67) Ravel, B.; Newville, M. ATHENA and ARTEMIS: interactive graphical data analysis using IFEFFIT. *Phys. Scr.* **2005**, *115*, 1007−1010.

(68) Altomare, A.; Giacovazzo, C.; Guagliardi, A.; Moliterni, A.G.G.; Rizzi, R.; Werner, P-E. Advances in powder diffraction pattern indexing: N-TREOR09. *J. Appl. Cryst.* **2000**, *33*, 1180–1186.

(69) Altomare, A.; Camalli, M.; Cuocci, C.; Giacovazzo, C.; Moliterni, A.; Rizzi, R. EXPO2009: structure solution by powder data in direct and reciprocal space. *J. Appl. Cryst.* **2009**, *42*, 1197–1202.

(70) Altomare, A.; Cuocci, C.; Giacovazzo, C.; Moliterni, A.; Rizzi, R.; Corriero, N.; Falcicchio, A. EXPO2013: a kit of tools for phasing crystal structures from powder data. *J. Appl. Cryst.* **2013**, *46*, 1231−1235.

(71) Toby, B.H.; Von Dreele, R.B. GSAS-II: the genesis of a modern open-source all purpose crystallography software package. *J. Appl. Cryst.* **2013**, *46(2)*, 544−549.

(72) Ziegenbalg, S.; Hornig, D.; Görls, H.; Plass, W. Cobalt(II)-based single-ion magnets with distorted pseudotetrahedral [N_2O_2] coordination: experimental and theoretical investigations. *Inorg. Chem.* **2016**, *55*, 4047−4058.

(73) https://www.nist.gov/pml/xcom-photon-cross-sections-database.

(74) Hamulic, D.; Milosev, I.; Lützenkirchen-Hecht, D. *Thin Solid Films* **2018**, *667*, 11−20.

(75) Wang, H.-Y., Hung, S.-F., Chen, H.-Y., Chan, T.-S., Chen, H. M., Liu, B. In operando identification of geometrical-site-dependent water oxidation activity of spinel Co_3O_4. *J. Am. Chem. Soc.* **2016**, 138, 36−39.

(76) Hörkner, W.; Müller-Buschbaum, H.K. Zur Kristallstruktur von $BaAl_2O_4$. *Z. Anorg. Allg. Chem.* **1979**, *451*, 40−44.

(77) Muncaster, G.; Sankar, G.; Richard, C.; Catlow, A.; Thomas, J.M.; Coles, S.J.; Hursthouse, M. The local structure of tetrahedral Co(III): A detailed crystal structure investigation of $K_5Co^{III}W_{12}O_{40} \cdot 20H_2O$. *Chem. Mater.* **2000**, *12*, 16–18.

(78) Beale, A.M.; Sankar, G.; Catlow, C.R.A; Anderson, P.A.; Green, T.L. Towards an understanding of the oxidation state of cobalt and manganese ions in framework substituted microporous aluminophosphate redox catalysts: An electron paramagnetic resonance and X-ray absorption spectroscopy investigation. *Phys. Chem. Chem. Phys.* **2005**, *7*, 1856–1860.

(79) Chmaissem, O.; Zheng, H.; Huq, A.; Stephens, P. W.; Mitchell, J.F. Formation of Co^{3+} octahedra and tetrahedra in $YBaCo_4O_{8.1}$. *J. Solid State Chem.* **2008**, *181*, 664–672.

(80) Baker, L.C.W; McCutcheon, T.P. Heteropoly salts containing cobalt and hexavalent tungsten in the anion. *J. Am. Chem. Soc.* **1956**, *78*, 4503–4510.

(81) Stötzel, J.; Lützenkirchen-Hecht, D.; Frahm, R.; Santilli, C.V.; Pulcinelli, S.H.; Kaminsky, R.; Fonda, E.; Villain, F.; Briois, V. QEXAFS and UV/Vis simultaneous monitoring of the TiO$_2$-nanoparticles formation by hydrolytic sol−gel route. *J. Phys. Chem. C* **2010**, *114*, 6228−6236.

(82) Lützenkirchen-Hecht, D.; Frahm, R. Corrosion of Mo in KOH: time resolved XAFS investigations. *J. Phys. Chem. B* **2001**, *105*, 9988–9993.

(83) Farges, F.; Brown, G.E.; Rehr, J.J.; Ti K-edge XANES studies of Ti coordination and disorder in oxide compounds: Comparison between theory and experiment. *Phys Rev B* **1997**, *56*, 1809.

(84) Ankudinov, A.L.; Ravel, B.; Rehr, J.J.; Conradson, S.D.; Real space multiple scattering calculation of XANES, *Phys. Rev. B* **1998**, *58*, 7565.

(85) Ankudinov, A.L.; Bouldin, C.; Rehr, J.J.; Sims, J.; Hung, H. Parallel calculation of electron multiple scattering using Lanczos algorithms. *Phys. Rev. B* **2002**, *65*, 104107.

(86) Shannon, R.D. Revised effective ionic radii and systematic studies of interatomic distances in halides and chalcogenides. *Acta Cryst. Sect. A: Cryst. Phys., Diffr.,Theor. Gen. Cryst.* **1976**, *32*, 751−767.

(87) Saber. M.R.; Dunbar, K.R.; Ligands effects on the magnetic anisotropy of tetrahedral cobalt complexes. *Chem. Commun.* **2014**, *50*, 12266–12269.

(88) Boča, R. Zero-field splitting in metal complexes. *Coord. Chem. Rev.,* **2004**, *248*, 757–815.

(89) Shimada, Y.; Miyasaka, S.; Kumai, R.; Tokura, Y. Semiconducting ferromagnetic states in La$_{1-x}$Sr$_{1+x}$CoO$_4$. *Phys. Rev. B,* **2006**, *73*, 134424.

(90) Chin Y.-Y.; Lin, H.-J.; Hu, Z.; Kuo, C.-Y.; Mikhailova, D.; Lee, J.-M.; Haw, S.-C.; Chen, S.-A.; Schnelle, W.; H. Ishii; Hiraoka, H. N.; Liao, Y.-F.; Tsuei, K.-D.; Tanaka,

A.; Tjeng, L.H.; Chen, C.-T.; Chen, J.-M. Relation between the Co–O bond lengths and

the spin state of Co in layered cobaltates: a high-pressure study. *Sci. Rep.* **2017**, *7: 3656*.

"For Table of Contents Only"
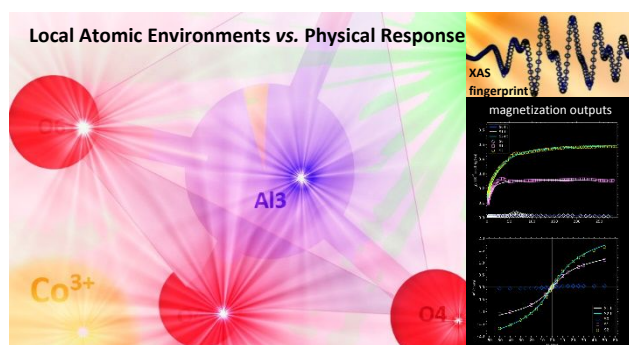
An effect of Co^{3+} dopant on the neighboring environment within the $BaAl_2O_4$ host lattice was spotlighted through a correlation of local atomic structure unveiled from X-ray absorption spectroscopy, and long-range ordering obtained from the Rietveld refinements. Simultaneous magneto-structural analysis of peculiar tetrahedral coordination unraveled in $Ba(Al_{0.998}Co_{0.002})_2O_4$ and $Ba(Al_{0.991}Co_{0.009})_2O_4$ powders shows that the subtle modifications of $BaAl_2O_4$ host by Co^{3+} give rise to the axial and rhombic ZFS terms, leading to larger anisotropy.